

Not to appear in Nonlearned J., 45.

## Optical and infrared color distributions in nearby early-type galaxies and the implied age and metallicity gradients

Hong Wu<sup>1,6</sup>, Zhengyi Shao<sup>2,6</sup>, H. J. Mo<sup>3,6</sup>, Xiaoyang Xia<sup>4</sup>, Zugan Deng<sup>5</sup>

hwu@bao.ac.cn

### ABSTRACT

We analyze the optical and near-infrared (NIR) surface photometries for a sample of 36 nearby early-type galaxies based on the eight broad-band images obtained from the Early Data Release (EDR) of the Sloan Digital Sky Survey (SDSS) and the Two Micron All Sky Survey (2MASS). The surface brightness profiles of most galaxies can be well fitted by the de Vaucouleur law, and the effective radius decreases significantly from blue optical to NIR bands. We also study the color gradients of each galaxy among all these eight bands. When transformed to the standard photometric system, the average color gradients in  $U - R$ ,  $B - R$  and  $J - K_S$  are  $-0.21$ ,  $-0.08$  and  $-0.09$ , respectively. With the use of simple stellar population (SSP) model, we interpret the observed color gradients in terms of the gradients in the metallicity and age of the stellar components in these galaxies. If age gradient is assumed to be absent, the observed color gradients implies a median metallicity gradient of  $-0.22$ , although the scatter is quite big among different galaxies. Fitting both age and metallicity simultaneously, and using  $g_Z = d \log Z_{\text{met}} / d \log R$  and  $g_A = d \log \text{Age} / d \log R$  to represent the metallicity and age gradients, we found that the median value  $g_Z = -0.24 \pm 0.03$

---

<sup>1</sup>National Astronomical Observatories, CAS, Beijing 100012, P.R. China

<sup>2</sup>Shanghai Astronomical Observatory, CAS, Shanghai 200030, P.R. China

<sup>3</sup>Astronomy Department, University of Massachusetts, Amherst MA 01003, USA

<sup>4</sup>Department of Physics, Tianjin Normal University, Tianjin 300074, P. R. China

<sup>5</sup>Graduate School, Chinese Academy of Sciences, Beijing 100080, P. R. China

<sup>6</sup>Max-Planck-Institut für Astrophysik, Karl Schwarzschild Str. 1, Postfach 1317, 85741 Garching, Germany

for the metallicity gradient, with a dispersion  $\sigma_{g_Z} = 0.20 \pm 0.02$ . The corresponding values for the age gradient are  $g_A = 0.01 \pm 0.04$  and  $\sigma_{g_A} = 0.23 \pm 0.03$ . These results are in good agreement with other observational results and with recent simulations that suggests both monolithic collapse and major merger may have played important roles in the formation of early-type galaxies. Our results also demonstrate the potential of using multi-waveband colors to be obtained from current and future optical and infrared surveys in constraining the age- and metallicity gradients in early-type galaxies.

*Subject headings:* galaxies: photometry - galaxies: metallicity - galaxies: age

## 1. Introduction

Color gradient of stellar light is a significant observational fact about early-type galaxies that has been known for quite a long time (de Vaucouleurs 1961; Boroson, Thompson & Shectman 1983). Such gradient is believed to be due to the variation of the properties of the underlying stellar population, such as age and metallicity. Theoretically, radial variation of metallicity is expected in some formation scenarios for early-type galaxies. Early simulations of monolithic collapse of a gas cloud tended to predict metallicity gradients that are too steep to match observations (e.g. Larson 1974; Carlberg 1984). Later theoretical considerations suggested that mergers of formed galaxies may have played an important role in the formation of early-type galaxies, and simulations with such scenario showed that the interaction between merging galaxies can effectively dampen the metallicity gradient in the progenitors (e.g. White 1980; Kobayashi 2004). Radial age gradient is also theoretically conceivable. For example, if stars in early-type galaxies were formed over an extended period in early star-forming galaxies in an inside-out fashion, and if later mergers of progenitors to form an elliptical galaxy did not result in a complete mixing of the stellar population, stars in the center of the elliptical galaxy would be older. On the other hand, if a formed elliptical could accrete gas into its center and form stars there, the stellar population in the center may appear younger. Clearly, accurate observational results are essential in distinguishing the different possibilities.

Evidence for radial metallicity gradient in early-type galaxies comes mainly from spectroscopic measurements of stellar absorption lines. Baum, Thomsen and Morgan (1986) first obtained a radial gradient in  $Mg$  for early-type galaxies in the Coma cluster. Using long-slit spectra of 42 nearby early-type galaxies, Carollo, Danziger and Buson(1993) found significant radial gradients in  $Mg$  and  $Fe$ . With the use of long-slit spectra of a sample of 13 elliptical and lenticular galaxies, Davies, Sadler & Peletier (1993) obtained an aver-

age gradient of  $\Delta[\text{Fe}/\text{H}]/\Delta \log R = -0.2 \pm 0.1$ , over the radius range  $0.1 \sim 1.0 R_{\text{eff}}$ . Based on the observational data obtained by González (1993) and Mehlert et al. (1998), with a sample of 60 early-type galaxies (40 elliptical and lenticular galaxies in the Coma cluster and 20 field elliptical galaxies), Henry & Worthey (1999) obtained  $\Delta \log Z/\Delta \log R \approx -0.25$ . More recently, Mehlert et. al. (2003) derived a metallicity gradient of  $-0.16 \pm 0.12$  from 35 early-type galaxies in the Coma cluster. There is also evidence that the gradient may become steeper for later type galaxies; for example , Fisher, Franx and Illingworth (1996) found  $\Delta[\text{Fe}/\text{H}]/\Delta \log R = -0.7 \pm 0.4$  for 20 S0 galaxies.

Although spectroscopic indices may be the most direct and best indicators of metallicity, it is not easy to build up a large sample for statistical analyses, because of the difficulties associated with obtaining long-slit (two-dimensional) spectra. Furthermore, the rapid decrease of surface brightness with radius also limits the radial range over which accurate spectroscopic measurements can be made. Such measurements are usually possible only up to a radius of about one effective radius, making it difficult to study gradients in the outer parts of elliptical galaxies. On the other hand, photometric measurements are much easier to obtain, and can easily cover a range of several effective radius. Thus, photometric measurements are still widely used for studying the metallicity and age gradients in early-type galaxies, although the interpretation of such measurements have to contend with the well-known age-metallicity degeneracy (e.g. Worthey 1994). Early analyses of nearby galaxies in the optical bands (Boroson, Thompson & Shectman 1983; Davis et. al. 1985; Cohen 1986; Franx, Illingworth & Heckman 1989; Peletier et al. 1990; Michard 1999; Scudiego 2001; Idiart, Michard & de Freitas Pacheco 2002) all indicated that early-type galaxies have shallow optical color gradients. This is supported by the more recent analysis of Tamura & Ohta (2003) based on the surface photometries of E/S0 galaxies in the nearby rich cluster Abell 2199. Similar results were obtained by Saglia et al. (2000) for the early-type galaxies in a cluster at redshift of about 0.4. Analyses about color gradients have also been carried out in NIR bands. The advantage of using NIR data is that dust contamination in such bands is less important, and the age-metallicity degeneracy is weaker (Worthey 1994), than that in optical bands. Silva and Elston (1994) investigated near-infrared color gradient for 8 early-type galaxies, and found that all of them show quite shallow gradients.

Because of the age-metallicity degeneracy in the color of stellar population (Worthey 1994), usually one can only estimate either the metallicity gradient or the age gradient by assuming the gradient of another quantity is known. Assuming the age of the stellar population to be the same over an entire galaxy, both Peletier, Valentijn & Jameson (1990) and Idiart, Michard & de Freitas Pacheco (2003) obtained a metallicity gradient of  $\sim -0.16$ . With the same assumption, Tamura & Ohta (2003) found a metallicity gradient  $-0.3 \pm 0.1$  based on 40 galaxies in Abell 2199 and 11 galaxies in Abell 2634. Using stellar population

synthesis model, Saglia et al. (2000) examined the origin of the color gradients by comparing 20 brightest early-type galaxies in CL0949+44 at redshift  $\sim 0.4$  from HST WF2 frames with local galaxies and concluded that their results are better explained in terms of metallicity gradient than in terms of age gradient. Similar results were obtained by Tamura et al. (2000) and Tamura & Ohta (2000) for elliptical galaxies in distant clusters with redshift from 0.37 to 0.56 based on HST WFPC2 deep images.

By studying Balmer line indices, people found that some ellipticals not only show metallicity gradients, but also age gradients, in the sense that the inner part is younger than the outer part (González 1993; Tantalo, Chiosi & Bressan 1998; Trager et al. 2000). Henry & Worthey (1999) quoted an average value of  $\Delta \log \text{Age}/\Delta \log R \approx 0.1$ . These results indicate that there may be additional star formation activities near the centers of these galaxies. However, current observations about this kind of age gradient are still quite uncertain. For example, by investigating the optical to NIR color gradients on HST WFPC2 and NICMOS images for six field early-type galaxies with redshift from 0.4 to 1.0, Hinkley & Im (2001) examined the possibility of a secondary star burst in the central parts of these galaxies, and found that 5 out of the 6 galaxies do not show any evidence for a bluer core.

In this paper, we use the broad band photometries obtained by the Sloan Digital Sky survey (SDSS) in optical, together with the 2 Micron All Sky Survey (2MASS) photometric data in the NIR, to study the color gradients for nearby early-type galaxies. The relative high image quality in both the SDSS and 2MASS surveys makes it possible to trace spectral energy distribution (SED) to the outer part of individual galaxies. In addition, since the combined SDSS and 2MASS data give a uniform coverage of the SEDs over a larger wavelength range, we may hope to use such data to derive stringent constraints on the variations of the stellar populations in early-type galaxies. In this paper, we present results based on 36 early-type galaxies. Although this sample is not larger than those used in early analyses, our results demonstrate the strength of combining SDSS and 2MASS data in studying stellar populations in early-type galaxies. In the future, much larger samples for such analyses can be obtained by matching galaxies in the 2MASS survey with those in the on-going SDSS survey.

The outline of the paper is as follows. We describe our galaxy sample and related data reduction in Section 2. In Section 3 we examine the surface brightness profiles of individual galaxies in each of the SDSS and 2MASS bands, and study the corresponding color gradients. In Section 4, we use the stellar population synthesis model to obtain constraints on the age and metallicity gradients. We discuss our results in Section 5, and conclude in Section 6. Except stated otherwise, we assume the Hubble constant to be  $H_0 = 70 \text{ km s}^{-1} \text{ Mpc}^{-1}$ .

## 2. Sample and data reduction

### 2.1. The Sample

The galaxy sample used in this work is selected from the Early Data Release (EDR) of the SDSS, which covers about  $462 \text{ deg}^2$  of the sky. More information about the EDR can be found in Stoughton et al. (2002). We select nearby galaxies that are brighter than 13.5 magnitude in the  $r$ -band, which guarantees that the sample galaxies all have bright and large images in all the SDSS and 2MASS bands. Since one of the main goals of this work is to use broad band photometries to disentangle the age-metallicity effects in the observed color gradients, accurate photometric measurements are required. We select 36 early-type galaxies (E,S0), where most of the morphological types are obtained from the literature (RC3 by de Vaucouleurs et al. 1991, NASA/IPAC Extragalactic Database, & Nakamura et al. 2003) and others are determined by us by inspecting their images in the SDSS. Since no other selection criterion was used except the magnitude limit, the sample is roughly a magnitude-limited sample of early-type galaxies. Table 1 lists, for each of the sample galaxy, the redshift, the morphological type from different sources, and the absolute magnitude in the  $B$ -band (which we deduce from the SDSS  $g$ -images together with the color correction given in eq.[2]).

For each of the sample galaxy, we extract the corrected images in the five SDSS bands ( $u$ ,  $g$ ,  $r$ ,  $i$  and  $z$ ) from the EDR archive imaging frames, which are produced by the SDSS pipeline with both photometric and astrometric calibrations (Stoughton, 2002). Each frame contains  $2048 \times 1489$  pixels, and the size of each pixel is  $0.396''$ . For point sources, the magnitude limits are 22.0, 22.2, 22.2, 21.3 and 20.5 for the  $u$ ,  $g$ ,  $r$ ,  $i$ ,  $z$ , respectively. NIR images in the  $J$  ( $1.25\mu\text{m}$ ),  $H$  ( $1.65\mu\text{m}$ ) and  $K_S$  ( $2.17\mu\text{m}$ ) bands are extracted from the 2MASS 2nd data release (Cutri, et al. 2000), according to the SDSS coordinates. In our following analyses, we will use the uncompressed atlas images provided by this data release. The pixel size of the 2MASS images are all  $1''$ , and the limits of the Vega-based magnitudes are 15.8, 15.1 and 14.3 for  $J$ ,  $H$ , and  $K_S$ , respectively.

### 2.2. Data reduction

#### 2.2.1. Preliminary data processing of the EDR images

Imaging processing in the five SDSS bands is originally performed by the photometric pipeline (PHOTO), which performs tasks such as labelling frame artifacts (bad columns, cosmic rays, bleed trails), bias subtraction, and flat-field correction. The astrometric solutions

Table 1: Sample of early-type galaxies from the SDSS EDR

object	redshift	$M_B$ mag	RC3 <sup>a</sup>	NFY <sup>b</sup>	NED <sup>c</sup>
ark402	0.0178	-20.01		1	
ark404	0.0187	-19.84		0	
cgcg010-030	0.0392	-21.32	0 S0/a	0	E
cgcg390-020	0.0374	-21.11			
gin 060	0.0443	-20.28			E
ic0590-1	0.0203	-19.69		0	E
ic0590-2	0.0209	-19.81		1	E
ic0891	0.0216	-20.16		0	
ic1517	0.0245	-20.63			
ic1639	0.0180	-20.08			cE
ngc0078b	0.0183	-19.79	-2 S0		S0 <sup>0</sup> pec?
ngc0359	0.0178	-20.11	-2 S0		S0-:
ngc0426	0.0175	-20.19	-4 E	0	E+
ngc0430	0.0177	-20.56	-5 E		E:
ngc0867	0.0213	-20.84	0 S0/a		S0+:
ngc0934	0.0212	-20.37	-2 S0		SAB0-:
ngc3325	0.0189	-20.75	-5 E		E:
ngc4044	0.0205	-20.48	-3 E-S0		E+:
ngc4493	0.0232	-20.51	-4 E	0	E+ pec:
ngc5865	0.0391	-21.83	-2 S0		SAB0-:
ngc5869	0.0070	-19.65	-2 S0		S0 <sup>0</sup> :
ngc6319	0.0275	-21.05			
ngc6359	0.0099	-19.45	-2 S0		SA0-:
ngc6382	0.0295	-21.00			
ngc6391	0.0276	-20.51			
ugc00588	0.0443	-21.67	0 S0/a		E
ugc00599	0.0436	-21.52			E/S0
ugc00797	0.0449	-21.56			cD;E:
ugc01072	0.0172	-19.63	-2 S0		S0
ugc05515	0.0443	-22.29	-4 E		E+ pec:
ugc06435	0.0254	-20.95	-2 S0	0	S0 <sup>0</sup> :
ugc07813	0.0232	-20.67	-5 E	0	E:
ngc0364	0.0170	-20.17	-2 S0		(R)SB(s)0 <sup>0</sup>
ngc0936	0.0048	-20.48	-1 S0-S0/a		SB(rs)0+:
ngc7684	0.0171	-20.35	0 S0/a		S0+:
ugc07177	0.0203	-19.99	-3 E-S0	0	S0-?

<sup>a</sup>Third Reference Catalogue of Bright Galaxies, de Vaucouleurs et al. 1991<sup>b</sup>From Nakamura et al (2003), 0: E; 1: S0<sup>c</sup>NASA/IPAC Extragalactic Database

for all the five bands are obtained by the astrometric pipeline (ASTROM), with typical error much smaller than  $0.1''$  (Stoughton et al. 2002), so that we can match accurately the images in any 2 bands of the SDSS and 2MASS. The astrometry accuracy of 2MASS is better than  $0.2''$  (Cutri, et al. 2000).

Although the images from the SDSS archive are processed with photometric corrections, some structures are still present in many image frames, especially for the  $u$  and  $z$  bands. The spatial variation of these structures is about 1 to 2 adu, which might be due to the bias structure of the CCDs. For galaxies which happen to be located in such structures, the variation can affect both the background subtraction and the measurement of color profile at the outer part of an image, where the surface brightness is low. Fortunately, most of these structures are only one dimensional, and the variation is just along the horizontal lines. So, it is not difficult to measure and then pick them out from images. To do this, we first select a region that includes several hundreds of lines, but covers all columns, and contains only a few faint objects. We then measure the median adu value of these lines in the selected region for every columns and use the obtained median values to represent the structures. Finally, we use the high order Spline3 function to fit them. The fitted structures are then subtracted from each line of the image. Figure 1 shows an example of such structures of an image in the  $u$ -band. The upper two panels show the plots of the averages of 500 lines at two different parts of the CCD frame, with the left panel for lines 1 to 500 while the right panel for lines 971 to 1470. As one can see, the structures in both panels are quite similar, indicating that these structures are quite systematic through the whole CCD frame. The lower two panels show the same plots as in the upper panels, except that the structures are now subtracted. One sees that the patterns are removed quite successfully by our method. In most cases, our subtraction method can reduce the spatial variation to a level  $\sim 0.2$  adu. Only for a few very large galaxies and for images with heavily saturated stars, where it is difficult to find a sufficiently large blank-line region for estimating the median value, such subtraction may fail to suppress the variation to such a low level.

### 2.2.2. *Surface photometry*

Since the FWHMs of the SDSS PSFs ( $\sim 1.5''$ ) are much smaller than those of the 2MASS ( $\sim 2.5''$ ), we down-grade the SDSS images by convolving with a proper gaussian kernel to match the 2MASS PSFs, so that we can obtain the SEDs also for the inner regions of galaxies with a similar seeing in different bands. Note that the SDSS PSF may change slightly from band to band, and the kernel used is in accordance with the specific filter and field in consideration. To obtain the true surface brightness profiles, an accurate sky background

subtraction is essential. For a given galaxy, we mask all other objects in the frame using SExtractor (Bertin & Arnouts 1996). Since most of the sample galaxies have sizes of a few arcmins, we can easily find enough sky region to fit the sky background reasonably well with a slope plane.

We use the ISOPHOTE Package in IRAF to fit each of the sky-subtracted images with a series of elliptical annuli from the center to the outskirt, with the length of the semi-major axis increased by 10% in each step. The width is chosen to increase with the radius of the annulus to suppress the noise in the outer region, where the signal-to-noise is low. Except the sky level, all other parameters (the coordinates of the center, ellipticity and position angle) are all treated as free parameters in the fit. Also, all of the foreground and background objects are masked out in order to reduce their contamination. Since our goal is to obtain the radial profile of the SED, we must make sure that each elliptical isophotic annulus has the same physical size for all the eight bands. To do this we use the  $r$ -band image to define the isophotic annuli, and use them for all the eight bands. Figure 2 shows the surface brightness profiles obtained for an example galaxy, NGC 0430.

Figure 3 presents the SED represented by the fluxes in the eight bands for an example galaxy NGC 4044 and shows how the SED changes with radius. For example, the offset of SEDs at  $3.00''$  and at  $17.12''$  is larger than  $\sim 0.5$  magnitude from the red end to the blue end, implying a color gradient in the sense that the stellar light becomes redder toward the central part. We will quantify such gradients in the following.

### 2.2.3. Error estimates

The photometric error for each annulus is estimated based on the systematic errors of sky subtraction (about 0.2 adu for each band) and the uncertainties in the isophotic aperture. The typical errors in the eight bands ( $u, g, r, i, z, J, H, K_S$ ) are 0.05, 0.01, 0.01, 0.01, 0.02, 0.07, 0.08, 0.11 mag, respectively, at a radius near  $R_{50}$ , where  $R_{50}$  is the radius within which 50% of the Petrosian flux is contained (see Stoughton et. al 2002 and Petrosian 1976 for details). In this paper, we use  $R_{50}$  at the  $r$ -band to scale the size of annulus.

Notice that the  $u$ -band data have larger error bars as the lower observational efficiency in this band. Meanwhile, as the 2MASS images are much shallower than the SDSS images, the profiles in the NIR bands cannot be measured as far as for the optical ones. This mismatch of depths in different bands limits the ranges over which the SED profiles can be measured reliably.

#### 2.2.4. Calibration

The SDSS magnitudes are quite close to the AB-magnitude system. The zero-point of magnitude for each frame can be obtained directly from the EDR catalogue, and the corrections to the AB system are -0.042, 0.036, 0.015, 0.013, and -0.002 for  $u$ ,  $g$ ,  $r$ ,  $i$ , and  $z$ , respectively (Blanton et al. 2003). The 2MASS zero-point in Vega magnitude system can be found in the atlas image header, we correct them to the AB magnitude by adding an offset of 0.89, 1.37 and 1.84 for  $J$ ,  $H$ , and  $K_S$ , respectively (Finlator et al., 2000). In addition, the dust extinction of the Milky Way is corrected for individual galaxies according to their galactic coordinates as provided by Schlegel, Finkbeiner & Davis (1998).

#### 2.2.5. Correction for the ‘red halo’ in the PSF wings

In addition to the normal photometric correction discussed above, there is another instrumental effect that affects our analyses on the surface photometries of the SDSS galaxies. Since the SDSS photometry survey used the thinned CCD for the  $u, g, r, i$  bands, there is an effect referred in the literature as the ‘red halo’ of the PSF wings (e.g. Michard 2002). This effect causes the extended wing of a red-band PSF to be much brighter than that in a blue-band. In the SDSS photometric system, the ‘red halo’ in the  $i$ -band is more obvious than that in the other bands (see Appendix).

Since most of sample galaxies have sizes about several arcmins and the ‘red halo’ effect appears prominent at about 10 to 50 arcsecs, it is a serious problem in surface photometric measurements. It not only affects the SEDs and the color gradients, but also affects the measurement of the effective radius for individual galaxies. As pointed out by Michard (2002) that the ‘red halo’ effect depends on both observational time and the field, it is difficult to obtain the PSF for each field. Therefore, we adopt an average PSF for the correction, by which the ‘red halo’ effect could not be completely removed for individual galaxies. To reduce this effect, when measuring the color gradients, we use the method described by Idiart, Michard & de Freitas Pacheco (2002) ; when fitting the SEDs, we simply discard the  $i$ -band data. The details for ‘red halo’ correction will be addressed in both the following section and in Appendix.

### 3. Radial profiles and Color gradients

#### 3.1. Radial profiles

We have obtained the radial surface brightness profiles at eight bands for sample galaxies. Considering all sample galaxies are early-type galaxies, we simply take the de Vaucouleur profile in the fitting:

$$I(R/R_e) = I_e \exp\{-7.67[(R/R_e)^{1/4} - 1]\}, \quad (1)$$

where  $R_e$  is the effective radius and  $I_e$  is the surface brightness at  $R_e$ . For the seeing effects become important on scales smaller than about two FWHMs. (e.g. Petetier et al. 1990; Baggett, Baggett & Andersons 1998; Franx, Illingworth & Heckman 1989; Tamura and Ohta 2003), therefore, we adopt an inner radius as  $0.4R_{50}$  ( $\sim 3'' - 5''$ ) for our analysis. Meanwhile, as the data become quite noisy at larger radius at  $u$ ,  $J$ ,  $H$  and  $K_S$  bands, we cut the outer radius at  $5R_{50}$ . Actually, the de Vaucouleur model works well for most of sample galaxies, except for a few exceptional cases, which seem to have either a disk or a distinct bar. When we perform the fitting, the interactive STSDAS (Space Telescope Science Data Analysis System) task NFIT1D is used, in which all data points are weighted according to their errors. The best parameters obtained in this way for the  $J$ ,  $H$  and  $K_S$  bands have larger error bars, because of the larger uncertainty in the data. An example of the fitted profiles is shown in Figure 2. The best fit effective radii are listed in Table 2 for all galaxies in each of the eight bands.

It is clear from Table 2 that the effective radius  $R_e$  decreases systematically from blue to red colors among all eight bands. This indicates that the surface brightness profiles are different in different bands and therefore there exists radial color gradient in these galaxies. Such variation can be also seen from Figure 4, where the histograms of the effective radius in the eight wavebands are plotted, with the median values indicated by the vertical lines. This result is consistent with that obtained by Bernardi et al. (2003) from a much larger sample of SDSS early-type galaxies. Figure 5 presents the correlation between effective radius in the optical  $g$ -band and the mean value of 3 NIR bands. There is a tight correlation for almost all galaxies in our sample. The solid line gives the best linear fit for such a correlation. As a comparison, the dash line shows where the two effective radii are equal. The effective radius of a galaxy in the NIR bands is about two thirds of that in the  $g$ -band, which is consistent with the result obtained by Rembold et al. (2002).

Notice from Figure 4 and Table 2 that the effective radii at  $i$ -band are abnormally larger. As we have discussed at section 2.2.5, the larger value may be caused by the ‘red halo’ of the  $i$ -band PSF. Since the  $i$ -band wing is more prominent than those in other bands in the

radius range from 10 to 50 arcsecs, which is almost the radius range we make the profile fitting, the net effect of the bright wing is to increase the value of the effective radius in the  $i$ -band.

### 3.2. Color gradients

To quantify the color gradients obtained, we adopt the linear least-square method to fit the color profiles. In the fitting we use only data points in the radius range from  $0.4R_{50}$  to  $5R_{50}$ . We express the color gradient as  $\Delta(m_1 - m_2)/\Delta \log R$  in order to compare with previous results obtained by Peletier et al. (1990) in the optical bands and by Silva & Elston (1994) in the infrared bands. As discussed above, the red-halo effect in the  $i$ -band affects the gradients in the  $r - i$  and  $i - z$  colors, the  $r - i$  color presents abnormal positive gradient, especially for galaxies with smaller sizes, in agreement with the result for  $V - I$  color gradient obtained by Michard (2002) and Idiart, Michard & de Freitas Pacheco (2002).

To correct this effect, we adopt the same method as Idiart, Michard & de Freitas Pacheco (2002). Since the PSFs in  $u$ ,  $g$ ,  $r$ ,  $z$  are in good agreement with each other (see Figure 13), we only make corrections for the colors involving the  $i$ -band, i.e.,  $r - i$  and  $i - z$ . We convolve the  $r$ -band image with the  $i$ -band PSF obtained in Appendix A and vice versa. This will get rid of the differences in the PSFs between these two bands, then we can obtain a ‘corrected’  $r - i$  color gradient, although it is based on an ‘enlarged’ PSF. The same procedure is carried out also for the  $i - z$  color gradient (see Appendix for details). As we use the average PSF over different fields, the above procedure could introduce some errors for individual galaxies. However, this will not affect our statistical results, because the PSF variations from field to field are small. A linear fit to each of these profiles is carried out, with each data point weighted according to the measured uncertainties. The average  $r - i$  and  $i - z$  gradients are now  $-0.04$  and  $-0.03$ , respectively, compared to the values of  $+0.04$  and  $-0.09$  before the correction.

Figure 6 shows the color gradients for three example galaxies: Ark 402, NGC 0867 and NGC 6359; six color gradients are presented for each galaxy from top to bottom in each column. Table 3 presents the slope values of six color gradients for all sample galaxies. The last line at Table 3 is the average slope values of each color gradients on all sample galaxies. It is clear from Figure 6 and Table 3 that all the six color gradients have negative values, indicating that the color appears bluer from inner regions to outer part for early-type galaxies. This result is in agreement with previous investigations for early-type galaxies (Vader et al. 1988; Franx, Illingworth & Heckman 1989; Peletier, Valentijn & Jameson 1990; Peletier et al. 1990; Goudfrooij et al. 1994; Tamura et al. 2000; Tamura & Ohta 2000).

Table 2: Effective radii in optical and NIR bands.

objects	R <sub>u</sub> kpc	R <sub>g</sub> kpc	R <sub>r</sub> kpc	R <sub>i</sub> kpc	R <sub>z</sub> kpc	R <sub>J</sub> kpc	R <sub>H</sub> kpc	R <sub>Ks</sub> kpc
ark402	7.70±0.52	7.04±0.11	5.79±0.06	5.32±0.03	4.60±0.06	3.63±0.17	3.27±0.15	3.18±0.16
ark404	3.37±0.06	2.88±0.01	2.85±0.01	3.04±0.01	2.51±0.01	2.40±0.06	2.23±0.04	2.37±0.13
cgcg010-030	6.21±0.18	6.48±0.10	6.11±0.07	6.07±0.09	5.12±0.10	4.31±0.14	5.25±0.17	4.02±0.16
cgcg390-020	5.07±0.17	5.12±0.04	4.86±0.02	5.19±0.04	4.08±0.04	4.17±0.09	3.78±0.07	3.82±0.08
gin060	7.60±0.66	4.31±0.06	3.91±0.02	4.05±0.02	3.39±0.06	2.95±0.20	3.19±0.20	2.62±0.24
ic0590-1	4.97±0.16	5.14±0.05	5.30±0.05	6.04±0.03	4.51±0.05	4.23±0.24	3.37±0.18	3.61±0.21
ic0590-2	6.23±0.20	5.10±0.08	4.90±0.08	6.29±0.06	4.42±0.08	3.51±0.20	3.40±0.19	3.53±0.20
ic0891	6.60±0.16	4.79±0.02	4.76±0.01	4.41±0.02	4.32±0.03	3.79±0.27	3.73±0.22	3.35±0.23
ic1517	3.52±0.08	2.50±0.02	2.43±0.02	2.56±0.01	2.46±0.03	2.31±0.09	2.41±0.08	2.10±0.08
ic1639	1.52±0.03	1.19±0.01	1.19±0.01	1.44±0.00	1.40±0.01	1.61±0.04	1.21±0.04	1.39±0.06
ngc0078b	4.27±0.10	4.04±0.07	3.72±0.06	4.34±0.03	3.24±0.05	2.54±0.07	2.69±0.07	2.50±0.08
ngc0359	10.30±0.63	10.29±0.18	10.72±0.15	10.70±0.17	7.94±0.20	4.90±0.37	5.13±0.36	4.15±0.38
ngc0426	2.47±0.06	3.24±0.02	3.53±0.02	3.63±0.01	2.35±0.02	2.39±0.10	2.56±0.10	1.82±0.08
ngc0430	3.91±0.06	2.98±0.02	2.86±0.01	2.95±0.01	2.82±0.02	2.70±0.10	2.58±0.10	2.42±0.10
ngc0867	6.23±0.39	5.86±0.04	5.80±0.03	5.50±0.02	5.28±0.07	4.59±0.26	4.47±0.23	4.63±0.30
ngc0934	4.15±0.08	3.13±0.02	3.02±0.01	2.63±0.00	2.60±0.02	2.28±0.09	2.18±0.07	1.88±0.07
ngc3325	4.24±0.08	4.05±0.02	3.89±0.02	4.67±0.05	3.77±0.03	3.54±0.11	3.43±0.08	3.22±0.10
ngc4044	7.09±0.17	6.17±0.02	6.17±0.02	6.38±0.02	5.23±0.03	4.20±0.16	4.34±0.15	4.26±0.20
ngc4493	39.48±2.61	30.30±0.44	29.26±0.38	31.72±0.33	23.36±0.38	15.47±1.74	19.84±1.80	17.10±2.02
ngc5865	19.52±0.96	18.25±0.18	15.50±0.08	14.15±0.07	12.77±0.14	8.24±0.37	7.37±0.26	7.52±0.38
ngc5869	3.09±0.06	3.02±0.01	2.84±0.01	2.91±0.01	2.59±0.01	2.65±0.08	2.50±0.07	2.44±0.09
ngc6319	9.60±0.26	6.95±0.03	6.24±0.02	6.69±0.04	5.79±0.05	5.59±0.21	4.70±0.20	4.58±0.19
ngc6359	2.30±0.04	2.23±0.01	2.14±0.01	2.28±0.01	1.93±0.01	1.88±0.04	1.92±0.04	1.61±0.04
ngc6382	8.61±0.23	7.23±0.05	7.27±0.04	6.46±0.02	6.04±0.06	6.67±0.17	6.39±0.17	5.80±0.16
ngc6391	5.91±0.22	4.31±0.02	3.39±0.02	3.31±0.02	3.65±0.03	3.67±0.11	3.59±0.09	3.50±0.11
ugc00588	12.43±0.36	13.13±0.11	11.77±0.07	13.93±0.09	10.80±0.15	9.37±0.38	9.35±0.35	8.68±0.43
ugc00599	13.79±0.66	13.68±0.12	12.98±0.09	13.00±0.05	12.41±0.20	10.28±0.48	9.68±0.32	8.88±0.47
ugc00797	19.68±1.21	18.84±0.19	18.08±0.11	17.85±0.13	16.94±0.32	11.43±0.69	12.45±0.64	11.05±0.74
ugc01072	6.18±0.21	4.76±0.05	4.80±0.04	5.40±0.04	4.68±0.08	5.83±0.31	6.04±0.31	5.46±0.34
ugc05515	41.44±2.42	37.25±0.34	36.45±0.29	30.65±0.18	28.07±0.40	19.90±1.33	17.73±1.10	22.18±1.85
ugc06435	5.07±0.15	5.36±0.02	5.76±0.03	5.90±0.02	4.25±0.03	3.78±0.15	3.45±0.11	3.34±0.14
ugc07813	5.04±0.20	5.51±0.05	5.47±0.04	5.30±0.03	4.23±0.06	3.33±0.17	3.49±0.14	2.64±0.14
ngc0364	4.24±0.17	4.51±0.02	4.01±0.04	4.08±0.02	4.44±0.05	3.64±0.21	2.92±0.15	3.60±0.23
ngc0936	4.31±0.04	4.64±0.02	4.42±0.01	4.71±0.04	4.13±0.02	3.71±0.05	3.63±0.05	3.46±0.06
ngc7684	13.69±0.27	9.13±0.05	8.47±0.04	10.31±0.04	9.42±0.07	10.39±0.34	11.80±0.42	11.72±0.61
ugc07177	11.38±1.06	11.96±0.10	11.91±0.06	12.84±0.08	11.13±0.18	8.72±0.90	11.60±1.11	9.34±1.05
Median	6.05	5.13	5.10	5.36	4.43	3.79	3.61	3.56

The errors quoted in the table include both the fitting error and the errors introduced by the uncertainty in the background determination of the two bands in consideration. The latter is the dominated one and can be calculated using method given in Silva & Elston (1994). As one can see from Table 3, the errors in  $d(u - g)/d \log R$ ,  $d(J - K_s)/d \log R$  and  $d(g - K_s)/d \log R$  are much larger than those in the other optical bands, because of the shallower photometries in the  $u$  and all NIR bands.

In order to transform the SDSS photometric data to the standard  $UBVRI$  system, we use the formula of Smith et al. (2002):

$$B = g + 0.47(g - r) + 0.17; \quad (2)$$

$$U - B = 0.75(u - g) - 0.83; \quad (3)$$

$$B - V = 1.02(g - r) + 0.20; \quad (4)$$

$$V - R = 0.59(g - r) + 0.11; \quad (5)$$

$$R - I = 1.00(r - i) + 0.21. \quad (6)$$

Based on the average color gradients given in Table 3, the average color gradients in  $U - B$ ,  $B - V$ ,  $V - R$  and  $V - I$  are  $-0.13 \pm 0.04$ ,  $-0.05 \pm 0.01$ ,  $-0.03 \pm 0.01$  and  $-0.07 \pm 0.01$  mag per dex in radius, respectively. The derived color gradients in  $U - R$  and  $B - R$  are  $-0.21 \pm 0.04$  and  $-0.08 \pm 0.01$  mag per dex in radius.

#### 4. Age and metallicity gradients

In the preceding section we have seen that significant gradients in optical and NIR colors exist for nearby early-type galaxies. In this section, we intend to use these results to constrain the age and metallicity of the underlying stellar population. Because of the age-metallicity degeneracy (Worley 1994), it is in general difficult to separate these two effects using only one broad-band color. Since we now have observations in eight bands from optical to NIR to probe the underlying SED, it is interesting to see if we can disentangle the age-metallicity degeneracy with such data. Here we use stellar population synthesis model to explore this. Since there is a strong 'red halo' effect from the  $i$ -band (see details in Appendix), which may distort the SED shape at this wavelength, we will not use the  $i$ -band in the modelling analysis of this section.

Table 3: The color gradients of early-type galaxies

objects	$d(u - g)/d \log R$	$d(g - r)/d \log R$	$d(r - i)/d \log R$	$d(i - z)/d \log R$	$d(J - Ks)/d \log R$	$d(g - Ks)/d \log R$
ark402	-0.12± 0.05	-0.22± 0.01	-0.08± 0.01	-0.05± 0.02	-0.14± 0.09	-0.74± 0.08
ark404	-0.22± 0.03	-0.02± 0.01	-0.03± 0.01	-0.05± 0.01	-0.05± 0.05	-0.10± 0.04
cgcg010-030	-0.15± 0.08	-0.04± 0.01	-0.03± 0.02	-0.02± 0.03	-0.10± 0.11	-0.26± 0.10
cgcg390-020	0.04± 0.06	-0.06± 0.01	-0.08± 0.01	-0.04± 0.02	-0.12± 0.06	-0.35± 0.05
gin060	-0.37± 0.07	-0.13± 0.02	-0.07± 0.02	-0.06± 0.02	-0.13± 0.09	-0.61± 0.07
ic0590-1	-0.18± 0.05	-0.06± 0.01	0.06± 0.01	-0.16± 0.01	-0.11± 0.10	-0.16± 0.08
ic0590-2	-0.23± 0.05	-0.03± 0.03	0.07± 0.02	-0.15± 0.02	0.00± 0.08	-0.22± 0.06
ic0891	-0.25± 0.05	-0.04± 0.02	-0.08± 0.01	-0.04± 0.02	-0.14± 0.09	-0.37± 0.06
ic1517	-0.16± 0.03	-0.01± 0.01	-0.06± 0.01	0.03± 0.01	-0.14± 0.04	-0.31± 0.03
ic1639	-0.01± 0.02	-0.02± 0.01	0.05± 0.01	0.01± 0.01	0.10± 0.11	0.03± 0.09
ngc0078b	-0.22± 0.03	-0.08± 0.01	0.01± 0.01	-0.06± 0.01	-0.08± 0.07	-0.35± 0.05
ngc0359	-0.29± 0.06	-0.03± 0.01	-0.03± 0.01	-0.03± 0.01	-0.17± 0.13	-0.34± 0.11
ngc0426	-0.07± 0.07	-0.05± 0.01	-0.07± 0.01	-0.03± 0.01	-0.28± 0.06	-0.46± 0.04
ngc0430	-0.23± 0.03	-0.04± 0.01	-0.07± 0.01	0.02± 0.01	-0.12± 0.03	-0.25± 0.03
ngc0867	-0.14± 0.07	-0.01± 0.01	-0.07± 0.01	0.03± 0.02	0.03± 0.09	-0.15± 0.07
ngc0934	-0.29± 0.03	-0.05± 0.01	-0.07± 0.01	-0.04± 0.01	-0.25± 0.05	-0.50± 0.03
ngc3325	-0.10± 0.04	-0.05± 0.01	-0.07± 0.01	0.04± 0.02	-0.10± 0.07	-0.16± 0.06
ngc4044	-0.18± 0.05	-0.05± 0.01	-0.06± 0.01	-0.05± 0.02	-0.01± 0.07	-0.36± 0.05
ngc4493	-0.35± 0.06	-0.07± 0.02	-0.04± 0.02	-0.06± 0.02	-0.01± 0.15	-0.36± 0.12
ngc5865	-0.32± 0.06	-0.07± 0.01	-0.09± 0.01	-0.06± 0.02	-0.10± 0.11	-0.47± 0.09
ngc5869	-0.06± 0.04	-0.04± 0.01	-0.03± 0.01	-0.05± 0.01	-0.09± 0.07	-0.19± 0.06
ngc6319	-0.09± 0.05	0.04± 0.02	-0.06± 0.01	-0.05± 0.02	-0.22± 0.07	-0.52± 0.05
ngc6359	-0.26± 0.03	-0.08± 0.01	-0.05± 0.01	-0.03± 0.01	-0.16± 0.03	-0.35± 0.02
ngc6382	-0.14± 0.05	-0.10± 0.01	-0.03± 0.01	-0.06± 0.01	-0.15± 0.07	-0.26± 0.05
ngc6391	-0.26± 0.04	-0.10± 0.01	-0.05± 0.01	0.01± 0.01	-0.04± 0.05	-0.24± 0.04
ugc00588	-0.18± 0.06	-0.04± 0.01	-0.04± 0.01	-0.10± 0.02	-0.11± 0.08	-0.33± 0.06
ugc00599	-0.20± 0.06	-0.05± 0.01	0.00± 0.01	-0.09± 0.02	-0.16± 0.08	-0.30± 0.06
ugc00797	-0.36± 0.09	-0.02± 0.01	-0.05± 0.01	0.08± 0.02	-0.05± 0.13	-0.22± 0.10
ugc01072	-0.15± 0.03	-0.03± 0.01	-0.04± 0.01	0.00± 0.01	-0.05± 0.07	-0.04± 0.05
ugc05515	-0.25± 0.07	-0.06± 0.01	-0.06± 0.01	0.00± 0.02	0.10± 0.12	-0.19± 0.09
ugc06435	-0.16± 0.05	-0.11± 0.01	-0.02± 0.01	-0.02± 0.02	-0.12± 0.08	-0.28± 0.06
ugc07813	-0.22± 0.05	-0.07± 0.01	-0.06± 0.01	0.02± 0.02	-0.16± 0.08	-0.34± 0.07
ngc0364	-0.07± 0.07	-0.04± 0.01	-0.03± 0.01	0.01± 0.02	-0.01± 0.09	-0.22± 0.07
ngc0936	-0.02± 0.02	-0.02± 0.01	-0.03± 0.01	-0.02± 0.01	-0.05± 0.03	-0.17± 0.03
ngc7684	-0.13± 0.02	-0.06± 0.01	-0.05± 0.01	0.04± 0.01	0.05± 0.07	-0.06± 0.06
ugc07177	-0.02± 0.12	0.01± 0.02	-0.04± 0.02	-0.01± 0.03	0.02± 0.20	-0.16± 0.15
Average	-0.18± 0.06	-0.05± 0.01	-0.04± 0.01	-0.03± 0.02	-0.09± 0.08	-0.29± 0.07

#### 4.1. Fitting the observed SEDs with spectral synthesis model

In this paper, we adopt the spectral synthesis code, Gissel01 (Galaxy Isochrone Synthesis Spectral Evolution Library, Bruzual & Charlot, 2001) to fit the observed SEDs represented by the seven band photometries (without the  $i$ -band). This library is a special version which includes the filters of SDSS and 2MASS bands, making it possible to obtain directly the magnitudes in the eight bands concerned here. This code can be used to produce high-resolution model spectra for a Simple Stellar Population (SSP) at different ages with 6 initial metallicities: 0.0001, 0.0004, 0.004, 0.008, 0.02( $\sim Z_\odot$ ) and 0.05. Spectra for other metallicities can be obtained by a linear interpolation of these 6 fundamental ones. The code assumes the ‘universal’ initial mass function (IMF) obtained by Kroupa (2001). In most of our discussions, we assume that stars in each of the sample galaxies are formed in an instantaneous burst. Once an IMF is chosen, the stellar population is completely determined by its age and metallicity. The sensitivity of our results on this assumption has been tested by considering a model where the stellar ages have a finite spread. (see section 4.2).

We use the standard  $\chi^2$  minimization to fit an observed SED with the synthesized spectra at different ages and metallicities. Because both optical and NIR data are used, the approach can put a stringent constraint on either metallicity or age, if the other is kept fixed. To demonstrate this, we generate test SEDs represented by the eight bands directly from the spectral synthesis model with given metallicities and ages. We assign to each model magnitude an observational error ( $\sigma_{\text{obs}}$ ) that is equal to the median observational error at  $R_{50}$  (defined in Section 2.2.3). In addition, we include in the error budget an uncertainty from the model itself ( $\sigma_{\text{mod}}$ ). Charlot, Worthey and Bressan (1996) estimated this uncertainty by comparing the colors obtained from different stellar evolutionary tracks and spectral libraries. To take this into account, we include a model error of 0.05 magnitude in all of our analysis. The combined error for each band is assumed to be the sum in quadrature,

$$\sigma^2 = \sigma_{\text{obs}}^2 + \sigma_{\text{mod}}^2. \quad (7)$$

We have made tests using other values of  $\sigma_{\text{mod}}$  in the range from 0.03 to 0.07 magnitude, and found that such a change does not affect our results significantly.

Figure 7 shows the contours of  $\Delta\chi^2 \equiv \chi^2 - \chi^2_{\text{min}}$  in the age-metallicity plane for the testing SEDs obtained by using different combinations of broad band photometries, with the crosses indicating the input values for the age and metallicity of the stellar population. From Figure 7(a), it is clear that using the combined SDSS and 2MASS data, the age and metallicity is constrained within a very narrow strip. If either the age or the metallicity is chosen as a fixed value, the other parameter can be determined with an error smaller than 10%. On the other hand, the very elongated narrow contours clearly show that the

age and metallicity are highly degenerate even with the use of the present data. Because of this, it is quite hard to estimate the age and metallicity separately for individual galaxies. Comparing Figure 7 (a) and (b), one can see that the exclusion of the  $i$ -band data does not have a big effect. A comparison between Figure 7 (c) and (d) shows that the inclusion of 2MASS data can significantly reduce the size of the contour, even though the error of the 2MASS data is quite large. Note that, the contours in Figure 7(b) are not much smaller than those in Figure 7(d), even though they are obtained with the use of magnitudes in three additional bands. Apparently, extending the wavelength coverage is more important than simply adding photometric bands. This is in agreement with the conclusion reached by Cardiel (2003) that the use of well-separated bandpasses can help disentangling the stellar population properties.

#### 4.2. The radial gradients of age and metallicity

To obtain the age and metallicity gradients from the observed color gradients, we assume that the SED for each projected annulus can be described by a single stellar population, and use the  $\chi^2$  fitting described above to determine its age and metallicity. To start with, we make the assumption that the observed color gradient is from either age or metallicity by fixing one of the two parameters (metallicity or age) at the best-fit value for  $R_{50}$ . We then model the gradient treating both the age and metallicity as free parameters.

Figure 8 shows the results of such analysis for the galaxy NGC 4044. Panel (a) shows the contour of  $\Delta\chi^2$  in the age-metallicity space for the annulus at  $R_{50}$ , while panel (b) shows the observed SED for this annulus together with the best model fit. It is clear from Figure 8 that the observed SED is well reproduced by a single burst model, and the  $\Delta\chi^2$  contour map looks similar to those for the testing galaxies shown in Figure 7. Panel (c) shows the best fit metallicity as a function of radius, where the stellar age is fixed to be 9.1 Gyr (the best fit age at  $R_{50}$ ) across the entire galaxy. A metallicity gradient is clearly seen here. The two vertical dashed lines indicate the radii  $0.4R_{50}$  and  $5.0R_{50}$ , within which the observational SEDs are not seriously affected by the seeing and have high enough signal-to-noise ratio. We will fit the gradient by a linear function of  $\log(R)$  within this radius range. Panel (d) shows the age profile where the metallicity is assumed to be a constant across the galaxy.

From panel (c) and (d) of Figure 8, one can see that the radial gradients of either metallicity or age can be well described as a linear relationship in logarithmic space. We therefore define two slopes,

$$g_Z \equiv \frac{d \log Z_{\text{met}}}{d \log R} \quad \text{and} \quad g_A \equiv \frac{d \log \text{Age}}{d \log R} \quad (8)$$

to characterize the gradients of metallicity and age, respectively. Fitting the observational data for each galaxy assuming either  $g_A$  or  $g_Z$  is zero, we obtain the distribution of  $g_Z$  or  $g_A$ , and the results are shown in Figure 9. All galaxies except NGC 6319 can be well fitted by this method. The SED of NGC 6319 cannot be fitted by any simple synthesis model, then we exclude this galaxy in our analyses. The median values for these 35 galaxies are  $g_Z \sim -0.22$  and  $g_A \sim -0.31$ , respectively.

In order to constrain the metallicity and age gradients simultaneously, we assume that these gradients for each galaxy can be described by linear relations in the log-log space with slopes  $g_Z$  and  $g_A$ . Here again, the quantities at the effective radius  $R_{50}$  of a galaxy are used as the zero point of the relations for the galaxy. For given values of  $g_Z$  and  $g_A$ , we can construct a model galaxy with stellar populations that are specified by the age and metallicity gradients. The values of  $g_Z$  and  $g_A$  can then be determined for each galaxy by matching the predicted SEDs at different radii with the observed ones. Also we use the  $\chi^2$  minimization to obtain the best-fit values of  $g_A$  and  $g_Z$ , and data points in the radius range from  $0.4R_{50}$  to  $5.0R_{50}$  are used in the fit. Figure 10 shows the contour maps of  $\Delta\chi^2$  in the  $g_A$ - $g_Z$  space for 2 example galaxies. We see that the constraints on  $g_Z$  and  $g_A$  are not equally stringent for different galaxies.

Figure 11 shows the best fitting values of  $g_Z$  and  $g_A$  for 35 sample galaxies. In order to obtain a statistical constraint on  $g_A$  and  $g_Z$  for the entire sample, we use the  $\Delta\chi^2$  contours for a galaxy to obtain a distribution function  $P(g_Z, g_A)$  for the galaxy, and sum over all galaxies to obtain a distribution function  $P(g_Z, g_A)$ . The contours of this distribution function are plotted in Figure 11. Figure 12 shows the projections of the distribution function along the two axes, and each of them can be fitted reasonably well by a gaussian profile. Based on this we obtain  $g_Z = -0.24 \pm 0.03$ ,  $\sigma_{g_Z} = 0.20 \pm 0.03$  and  $g_A = 0.01 \pm 0.04$ ,  $\sigma_{g_A} = 0.23 \pm 0.03$ . Note that the contours shown in Figure 11 are elongated along the line of age-metallicity degeneracy, and so it is likely that the dispersions in  $g_A$  and  $g_Z$  are dominated by this degeneracy. Since the best-fit value for  $g_A$  is close to zero, the result is consistent with the assumption that all the observed gradients in the SEDs of early-type galaxies are due to metallicity variations. Indeed, the median value of  $g_Z$  obtained here is consistent with that obtained above with the assumption of  $g_A \equiv 0.0$ . The result is, however, not consistent with the assumption that all the gradients are due to age variations.

The above results are based on the assumption that stars in an elliptical galaxy were formed by an instantaneous burst with zero age spread. An important question is how sensitive the results are to this assumption. To do this, we consider other models in which the star formation rate in a galaxy changes with time as  $\text{SFR} \propto \exp(-t/\tau)$ , where  $\tau$  is a constant characterizing the spread in the ages of the stellar population. As illustration,

we consider three cases where  $\tau$  is equal to 0.5, 1.0 and 2.0 Gyrs, respectively. Note that the SSP considered above corresponds to  $\tau = 0.0$ . In such models, the two parameters that characterize the stellar population are the initial metallicity and starting time for star formation. We use the same procedure as for the SSP case to determine the median and dispersion for  $g_Z$  and  $g_A$ , and the results are listed in Table 4, along with the results for the SSP ( $\tau = 0$ ) case. Clearly, our conclusions about the age and metallicity gradients are quite insensitive to the assumption of the spread of stellar age. We have made calculations with even larger  $\tau$ , and found that significant difference occurs when  $\tau$  becomes larger than 8 Gyr.

## 5. Discussion

### 5.1. The effect of dust

It must be kept in mind that the results presented above have neglected any dust absorption from the host galaxies. Since dust obscuration reddens stellar light, the existence of dust may also produce color gradient in galaxies. It is well known that many elliptical galaxies contain a significant amount of interstellar medium (Roberts et al. 1991). Most of the gas is in the form of hot X-ray gas, and a small fraction (about  $10^7 M_\odot$ ) is in the form of dust (Kormendy & Djorgovski 1989; Forbes 1991; Goudfrooij 1994; Wise & Silva 1996). van Dokkum and Franx (1995) used HST images to study the dust properties from a sample of 64 early-type galaxies, and found that 48% of the galaxies show nuclear dust absorption. These results suggest that although dust is commonly found in elliptical galaxies, it is likely to be concentrated in the nuclear regions. Since our galaxies are large and we have excluded data within  $0.4 R_{50}$  from the centers of galaxies, the existence of nuclear dust should not affect our results significantly. Wise and Silva (1996) constructed a dust model for elliptical galaxies to study the effect of dust obscuration on broad band color gradients. The model assumes a spherically symmetric distribution of dust, with dust density changing with radius

Table 4: Metallicity and Age gradients and their dispersions obtained with different star formation time scales

	$g_Z$	$\sigma_{g_Z}$	$g_A$	$\sigma_{g_A}$
SSP	$-0.24 \pm 0.03$	$0.20 \pm 0.03$	$0.01 \pm 0.04$	$0.23 \pm 0.03$
$\tau = 0.5Gyr$	$-0.24 \pm 0.03$	$0.20 \pm 0.02$	$0.04 \pm 0.04$	$0.20 \pm 0.03$
$\tau = 1.0Gyr$	$-0.26 \pm 0.04$	$0.22 \pm 0.03$	$0.04 \pm 0.03$	$0.18 \pm 0.02$
$\tau = 2.0Gyr$	$-0.26 \pm 0.04$	$0.25 \pm 0.04$	$0.03 \pm 0.03$	$0.17 \pm 0.02$

as  $R^{-1}$ . They concluded that their dust model together with the dust mass inferred from IRAS observations can reproduce the observed color gradient. However, since many of the IRAS detections were made with a  $\sim 3\sigma$  threshold, it turned out that only 12 – 17% of the observed elliptical galaxies are detected with a sufficiently high confidence level (Bregman et al. 1998). If we adopt Wise and Silva’s preferred model and apply it to the averaged color gradients we have obtained, namely  $-0.21 \pm 0.04$ ,  $-0.08 \pm 0.01$  and  $-0.09 \pm 0.08$  mag per dex for  $U - R$ ,  $B - R$  and  $J - K_S$ , respectively, the dust absorption optical depth inferred are  $0.75 \pm 0.15$ ,  $0.45 \pm 0.06$  and  $1.21 \pm 1.16$ . There is only a mild discrepancy among different colors, and so we cannot rule out that dust obscuration contributes significantly to the observed color gradients. Thus, the effects of dust extinction on the color gradients are still open.

## 5.2. Comparison with earlier results

### 5.2.1. Color gradients

In order to compare our results with those from earlier analyses, we have transformed the SDSS photometric system to the standard  $UBVRI$  system using eqs.(2)-(6) and obtained the color gradients in standard system. In Table 5 we list the color gradients so obtained along with the results obtained from earlier analyses. Our  $U - B$ ,  $B - V$ ,  $V - R$  and  $V - I$  color gradients are in very good agreement with those obtained by Idiart, Michard & de Freitas Pacheco (2002) using 36 early-type galaxies and by Michard (2000) re-analyzing 30 ellipticals obtained from literature. The  $U - R$  and  $B - R$  color gradients were derived by Peletier et al. (1990) from 39 ellipticals, and by Franx and Illingworth (1990) from 17 ellipticals; the  $B - R$  color gradients were also obtained by Tamura & Ohta (2003) from galaxies in clusters Abell 2199 and Abell 2634. Our results are consistent with all these results.

Table 5: Comparison of color gradients

	$(U - B)$	$(B - V)$	$(V - R)$	$(V - I)$	$(U - R)$	$(B - R)$
This work	$-0.13 \pm 0.04$	$-0.05 \pm 0.01$	$-0.03 \pm 0.01$	$-0.07 \pm 0.01$	$-0.21 \pm 0.04$	$-0.08 \pm 0.01$
Idiat(2002)	$-0.13 \pm 0.04$	$-0.07 \pm 0.02$	$-0.02 \pm 0.01$	$-0.05 \pm 0.03$		
Michard(2000)	$-0.15 \pm 0.05$	$-0.06 \pm 0.03$	$-0.02 \pm 0.03$	$-0.05 \pm 0.02$		
Peletier(1990)					$-0.20$	$-0.09$
Franx(1990)					$-0.23 \pm 0.03$	$-0.07 \pm 0.01$
Tamura(2003)						$-0.09 \pm 0.04$

### 5.2.2. Metallicity and age gradients

The average value of the metallicity gradient,  $-0.24 \pm 0.03$ , and the dispersion,  $0.20 \pm 0.02$ , we obtained are in good agreement with previous results based either on spectroscopic measurements (Mehlert et al. 1998, 2003; Henry & Worthey 1999) or on photometric measurements (Peletier et al. 1990; Idiart, Michard & de Freitas Pacheco 2003; Tamura et al. 2000; Tamura & Ohta 2000; 2003). It is interesting to note that, although we use only photometric data, the distribution of  $g_Z$  and  $g_A$  we obtained is similar to that obtained from spectroscopic analyses. For example, comparing our Figure 11 with Figure 11(b) presented in Henry & Worthey (1999), we see that both plots show distributions that are elongated along the age-metallicity degeneracy line, and that the scatter around the degeneracy line is quite large ( $\sim 0.2$ ). There is, however, a noticeable difference: Henry & Worthey obtained an average age gradient of about 0.1, which is about  $2\sigma$  away from the median age gradient we have obtained. Note that in our analyses we have excluded the inner parts of galaxies, so that the existence of young nuclear disks is not taken into account, while the results presented in Henry & Worthey may include the inner parts of galaxies. Thus, this difference may not be an inconsistency between the two results.

## 5.3. Theoretical implications

Simulations of formation of ellipticals through monolithic collapse (Carlberg 1984, Kobayashi 2004) show that the metallicity gradient predicted by this model is quite steep, with  $g_Z \sim -0.5$  smaller. This is clearly in conflict with our result,  $g_Z \sim -0.24$ . On the other hand, recent simulations of Kobayashi (2004) showed the metallicity gradient can be significantly flattened by mergers. They showed that galaxies formed through minor mergers have an average metallicity gradient  $\Delta \log Z / \Delta \log R \sim -0.3$ , while galaxies formed through major mergers have  $\Delta \log Z / \Delta \log R \sim -0.2$  and none of them have gradient steeper than -0.35. Our results are in good agreement with these simulation results.

The average value of the age gradient we found,  $g_A \sim 0.0$ , suggests that stars over a wide range of radius (from 0.4 to  $5.0 R_{50}$ , as considered in this paper) in an early-type galaxy have approximately the same age. This is consistent with the monolithic scenario where the bulk of stars in a galaxy formed through a single burst. In the hierarchical scenario where galaxies formed through mergers, the lack of significant age gradient in early-type galaxies suggests that stars in these galaxies formed early in progenitors and that there must be some processes to prohibit subsequent star formation in the progenitors of early-type galaxies.

## 6. Summary

In this paper, we analyze the optical and NIR surface photometries for a sample of 36 nearby early-type galaxies based on eight broad-band images obtained from the SDSS and the 2MASS. We study the color gradients of each galaxy in all the eight bands, and model them in terms of the metallicity and age gradients of the underlying stellar populations. Our main results are summarized as follows.

1. The effective radius of an early-type galaxy decreases systematically from blue to red bands, indicating that the stellar population becomes bluer at larger radius.
2. Almost all galaxies show shallow color gradients in both the five SDSS bands and the three 2MASS bands. The corresponding average color gradients of  $U - R$ ,  $B - R$  and  $J - K_S$  are  $-0.21$ ,  $-0.08$  and  $-0.09$ , respectively, in agreement with previous results.
3. Fitting both the age and metallicity simultaneously with the stellar population synthesis model, and using  $g_Z = d \log Z_{\text{met}} / d \log R$  and  $g_A = d \log \text{Age} / d \log R$  to represent the metallicity and age gradients, we found that a median value  $g_Z = -0.24 \pm 0.03$  for the metallicity gradient, with a dispersion  $\sigma_{g_Z} = 0.20 \pm 0.02$ . The corresponding values for the age gradient are  $g_A = -0.01 \pm 0.04$  and  $\sigma_{g_A} = 0.23 \pm 0.03$ . These results are in good agreement with other observational results and with the expectations of the current theory of galaxy formation.

Given the amount of data now available from the 2MASS and current SDSS and to be available from the SDSS future observations and SIRTF, one can easily come up with a sample of several hundred large early-type galaxies to carry out the same analyses as presented in this paper. With such a sample, we can hope to study the age-metallicity gradients in early-type galaxies in unprecedented detail.

## 7. Acknowledgements

The authors thanks Ivan Baldry, Stephen Charlot, Daniel Thomas, Claudia Maraston, Luis Ho, Shude Mao, Guinevere Kauffmann, Jiasheng Huang, J. Mo, Shiyi Shen, Zhenlong Zou, Jingyao Hu and Hongjun Su for their helpful advice and discussions. This project is supported by NSF of China No.10273012, No.10273016, No.10333060 and NKBRSP G19990754.

Funding for the creation and distribution of the SDSS Archive has been provided by the Alfred P. Sloan Foundation, the Participating Institutions, the National Aeronautics

and Space Administration, the National Science Foundation, the U.S. Department of Energy, the Japanese Monbukagakusho, and the Max Planck Society. The SDSS Web site is <http://www.sdss.org/>. The SDSS is managed by the Astrophysical Research Consortium (ARC) for the Participating Institutions. The Participating Institutions are The University of Chicago, Fermilab, the Institute for Advanced Study, the Japan Participation Group, The Johns Hopkins University, Los Alamos National Laboratory, the Max-Planck-Institute for Astronomy (MPIA), the Max-Planck-Institute for Astrophysics (MPA), New Mexico State University, Princeton University, the United States Naval Observatory, and the University of Washington.

This publication makes use of data products from the Two Micron All Sky Survey, which is a joint project of the University of Massachusetts and the Infrared Processing and Analysis Centre/California Institute of Technology, funded by the Aeronautics and Space Administration and the National Science Foundation.

### A. Red halo of PSF wings of SDSS images

Michard (2002) studied the PSFs of thinned CCD in different bands, he concluded that the atmospheric seeing dominates the central range of PSF and the seeing effect disappears around  $15''$ . However, in the outer region, the wing of PSF is controlled by both instrumental and atmospheric scattering. The extended wing of red band of PSF is much brighter than that of blue band in thinned CCD, which is referred to as the "red halo" effect (Michard 2002; Idiart, Michard & de Freitas Pacheco 2002).

The SDSS project employs 30 Tektronix/SITe  $2048 \times 2048$  CCDs in a 5 by 6 array for the five bands, with 6 unthinned frontside CCDs for  $z$ -band and 24 thinned backside CCDs for the other four bands. To explore the outer PSF wings in these five bands, we selected isolated unsaturated and saturated stars in different EDR fields. All of these fields are sky subtracted (see section 2.2.2 for details) and the median intensity are measured in concentric circles around each star to avoid the effect of asymmetric features of saturated stars, and of foreground and background objects. The profiles of all stars for each band are scaled and combined within their proportional radial range. Then we obtained the mean PSF profiles in the five bands and constructed the PSF images according to the symmetry of the rotation axis.

Figure 13 shows the radial profiles of the mean PSFs of the five bands. The red halo problem is clearly seen here. The  $i$ -band profile is quite different from the other four bands at radius starting from about  $6''$  (consistent with Michard's result in 2002), and so the red

halo effect is expected to affect the surface brightness profiles of galaxies at radius larger than  $\sim 10''$ . The PSF profiles in the  $g$ ,  $r$ ,  $z$  bands agree very well with each other. Although  $z$ -band is much redder than  $i$ -band, there is no red halo problem in it, because unthinned CCDs are used. This confirms that the red halo effect only appears in thinned CCDs. The PSF of  $u$ -band is slightly higher than those of  $g$ ,  $r$ ,  $z$  bands, but much lower than that of the  $i$ -band. In this paper we neglect the small difference between  $u$ -band and  $g$ ,  $r$ ,  $z$  bands.

To get rid of the red halo effect in the color gradients, which involve the  $i$ -band ( i.e.  $r - i$  and  $i - z$ ), for individual galaxy, we adopt the method as in Idiart, Michard & de Freitas Pacheco (2002). We convolve the  $r$ -band image with the  $i$ -band PSF and vice versa. We re-measure the  $r - i$  profile based on these two convolved images. This will cancel the differences of the PSFs between these two bands and so we can obtain a ‘corrected’  $r - i$  color profile. The same procedure is carried out also for the  $i - z$  color profiles. Figure 14 gives one example of such a correction. After the correction the  $r - i$  color gradient changes from positive to negative. The abnormal positive gradient can therefore be completely attributed to the ‘red halo’ effect in the  $i$ -band. The  $i - z$  profile becomes much flatter after the correction. The amount of correction depends on the size and shape of the galaxy in consideration; it is larger for smaller and more elongated galaxies, consistent with the finding of Michard (2002).

## REFERENCES

Baggett, W.E., Baggett, S.M., & Anderson, K.S.J. 1998, AJ, 116, 1626  
Baum, W.A., Thomsen, B., & Morgan, B.L. 1986, ApJ, 301, 83  
Bernardi, M., et al. 2003, AJ, 125, 1882  
Bertin, E., & Arnouts, S. 1996, A&AS, 117, 393  
Blanton, M.R., et al. 2003, ApJ, 594, 186  
Boroson, T.A., Thompson, I.B., & Shectman, S.A. 1983, AJ, 88, 1707  
Bregman, J.N., Snider, B.A., Grego, L., & Cox, C.V. 1998, ApJ, 499, 670  
Bruzual, G., & Charlot, S. 2001, Galaxy Isochrone Synthesis  
Cardiel, N., Gorgas, J., Sánchez-Blázquez, P., Cenarro, A. J., Pedraz, S., Bruzual, G., Klement, J. 2003, A&A, 409, 511  
Carlberg, R.G. 1984, ApJ, 286, 416

Carollo, C.M., Danziger, I.J., & Buson , L. 1993, MNRAS, 265, 553

Charlot, S., Worthey, G., Bressan, A. 1996, ApJ, 457, 625

Cohen, J.G. 1986, AJ, 92, 1039

Cutri, R.M., et al. 2000, Explanatory Supplement to the 2MASS Second Incremental Data Release (Pasadena: Caltech)

de Vaucouleurs, G. 1961, ApJS, 5, 223

de Vaucouleurs G., de Vaucouleurs A., Corwin H.G., Buta R.J., Paturel G., & Fouque P. 1991  
Third Reference Catalogue of Bright Galaxies (RC3), Springer-Verlag: New York

Davies, R.L., Sadler, E.M., & Peletier, R.F. 1993, MNRAS, 262, 650

Davis, L.E., Cawson, M., Davies, R.L., Illingworth, G. 1985, AJ, 90, 169

Finlator, K., et al. 2000, AJ, 120, 2615

Fisher, D., Franx, M., & Illingworth, G. 1996, ApJ, 459, 110

Forbes, D.A. 1991, MNRAS, 249, 779

Franx, M., Illingworth, G., & Heckman, T. 1989, AJ, 98, 538

Franx, M., & Illingworth, G. 1990, ApJ, 359, L41

González, J.J. 1993, Ph.D. thesis, Univ. California, Santa Cruz

Goudfrooij, P., Hansen, L., Jorgensen, H.E., Norgaard-Nielsen, H.U., de Jong, T., & van den  
Hoek, L.B. 1994, A&AS, 104, 179

Henry, R.B.C., Worthey, G. 1999, PASP, 111, 919

Hinkley, S., Im, M. 2001, ApJ, 560, L41

Idiart, T.P., Michard, R., & de Freitas Pacheco, J.A. 2002, A&A, 383, 30

Idiart, T.P., Michard, R., & de Freitas Pacheco, J.A. 2003, A&A, 398, 949

Kobayashi, C. 2004, MNRAS, 347, 740

Kormendy, J., & Djorgovski, S. 1989, ARA&A, 27, 235

Kroupa, P. 2001, MNRAS, 322, 231

Larson, R.B. 1974, MNRAS, 166, 585

Mehlert, D., Bender, R., Saglia, R.P., & Wegner, G. 1998, in A New Vision of an Old Cluster: Untangling Coma Berenices, ed. A. Mazure, F. Casoli, F. Durret, & D. Gerbal (Singapore: World Scientific), 107

Mehlert, D., Thomas, D., Saglia, R.P., Bender, R., & Wegner, G. 2003, A&A, 407, 423

Michard, R. 1999, A&AS, 137, 245

Michard, R. 2000, A&A, 360, 85

Michard, R. 2002, A&A, 384, 763

Nakamura, O., et al. 2003, AJ, 125, 1682

Peletier, R.F., Davies, R.L., Illingworth, G.D., Davis, L.E., & Cawson, M. 1990, AJ, 100, 1091

Peletier, R.F., Valentijn, E.A., & Jameson, R.F. 1990, A&A, 233, 62

Rembold, S.B., Pastoriza, M.G., Ducati, J.R., Rubio, M., & Roth, M. 2002, A&A, 391, 531

Petrosian, V. 1976, ApJ, 209, L1

Roberts, M.S., Hogg, D.E., Bregman, J.N., Forman, W.R., & Jones, C. 1991, ApJS, 75, 751

Saglia, R.P., Maraston, C., Greggio, L. , Bender, R., & Ziegler, B. 2000, A&A, 360, 911

Schlegel, D.J., Finkbeiner, D.P., & Davis, M. 1998, ApJ, 500, 525

Scuderi, M. 2001 AJ, 121, 2413

Silva, D.R., & Elston, R. 1994, ApJ, 428, 511

Smith, J.A., et al. 2002, AJ, 123, 2121

Stoughton, C., et al. 2002, AJ, 123, 485

Tamura, N., & Ohta, K. 2000, AJ, 120, 533

Tamura, N., Kobayashi, C., Arimoto, N., Kodama, T., & Ohta, K. 2000, AJ, 119, 2134

Tamura, N., & Ohta, K. 2003, AJ, 126, 596

Tantalo, R., Chiosi, C., & Bressan, A. 1998, A&A, 333, 419

Trager, S.C., Faber, S.M., Worthey, G., & González, J.J. 2000, AJ, 119, 1645

Vader, J.P., Vigroux, L., Lachieze-Rey, M., & Souviron, J. 1988, A&A, 203, 217

van Dokkum, P.G., & Franx, M. 1995, AJ, 110, 2027

White, S.D.M. 1980, MNRAS, 191, 1

Wise, M.W., & Silva, D.R. 1996, ApJ, 461, 155

Worthey, G., 1994, ApJS, 95, 107

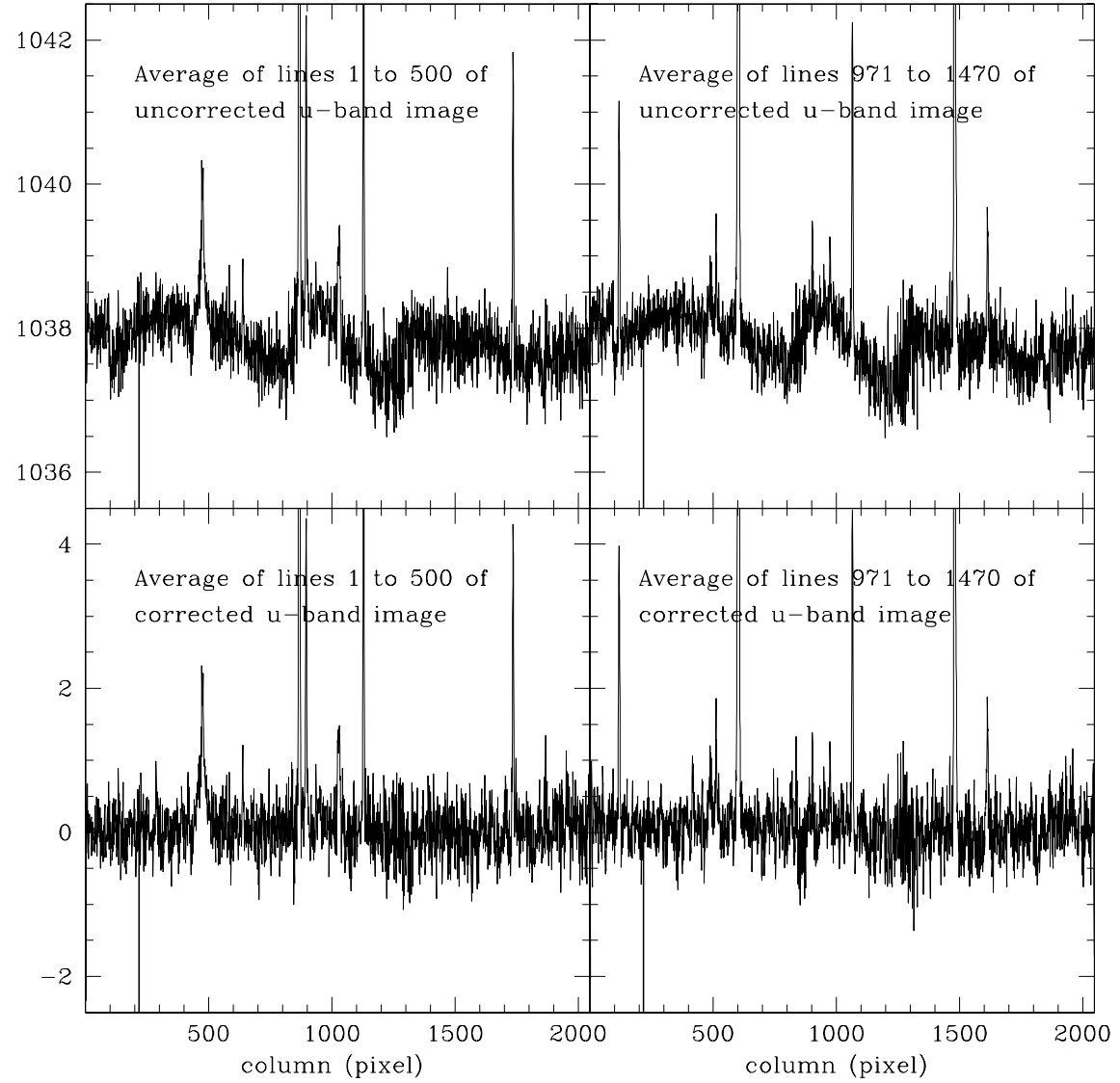


Fig. 1.— The upper two panels show the plots of the averages of 500 lines, at upper and lower parts of one SDSS imaging frame that presents the clear structures. The lower two panels show the corresponding corrected average plots. Note that these structures are removed successfully by our method.

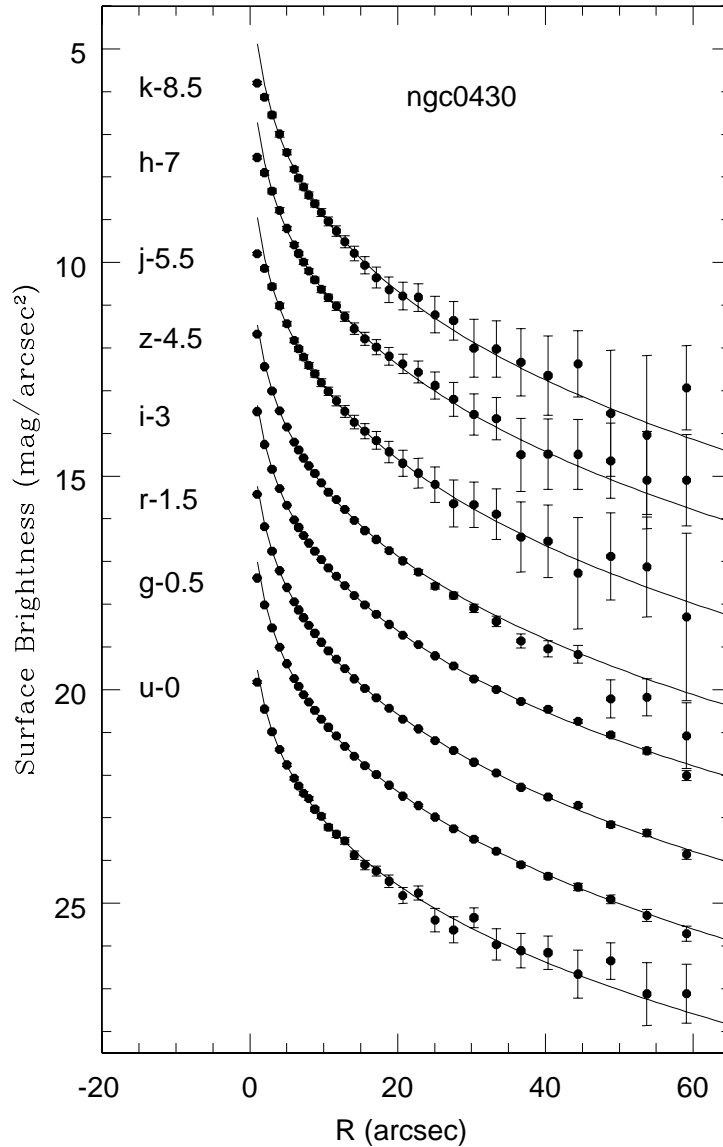


Fig. 2.— The measured surface brightness profiles for NGC 0430 as a function of radius in optical and NIR bands. The profiles are shifted for clarity. The error bars, defined in the text, are also plotted for each measured point. The curves are the best fit de Vaucouleur profiles.

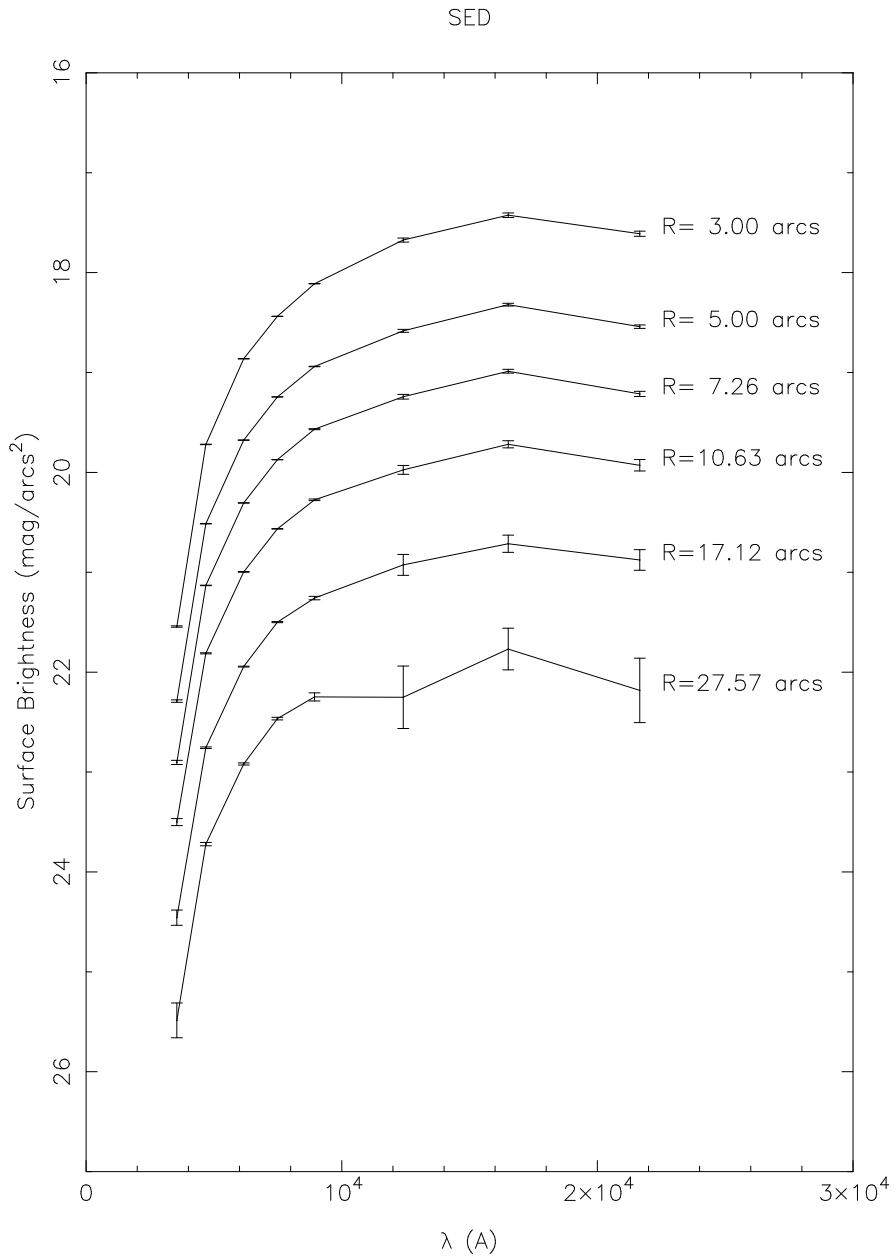


Fig. 3.— The SED of NGC 4044 at different radii as represented by the fluxes in eight bands. The value of  $R_{50}$  for this galaxy is 6.9" in the  $r$ -band.

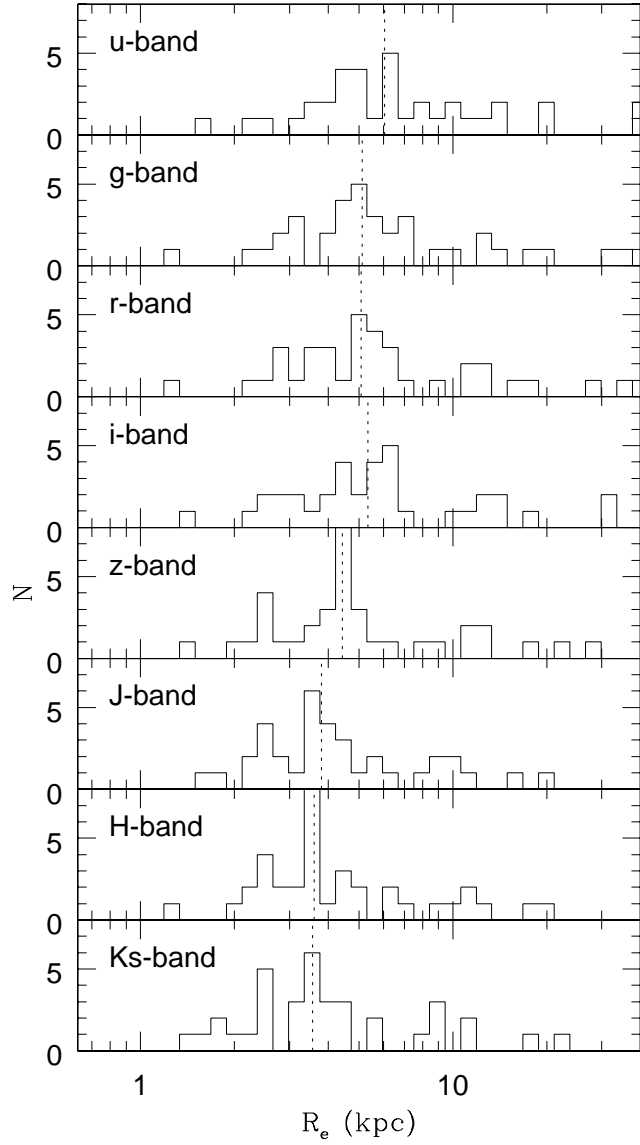


Fig. 4.— The histograms of the effective radii of sample galaxies in the optical and NIR bands. The vertical dotted line in each panel shows the median effective radius for each band. Note that the median value generally decreases with wavelength. The *i*-band is an exception, because of the red halo effect.

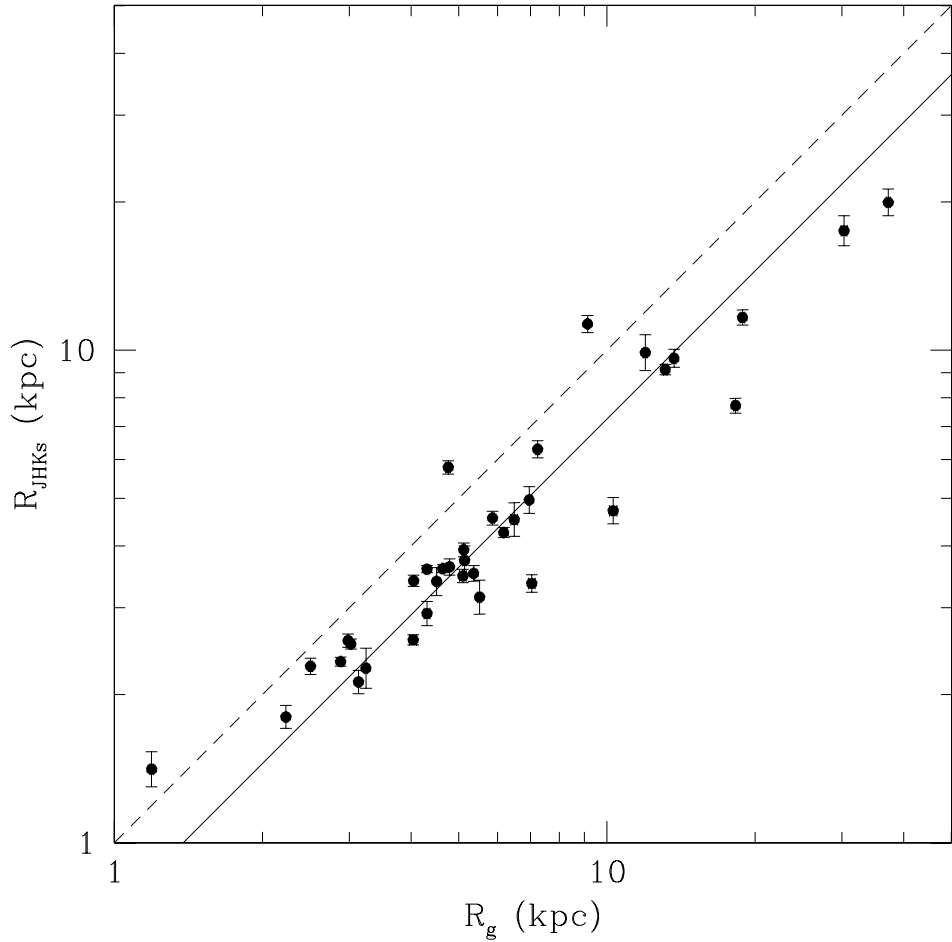


Fig. 5.— The correlation between the effective radii in optical and averaged NIR bands. The solid line is the best linear fit to the correlation and the dash line shows where the effective radii are equal. Note that the effective radius in the NIR band is generally about two thirds of that in the optical band.

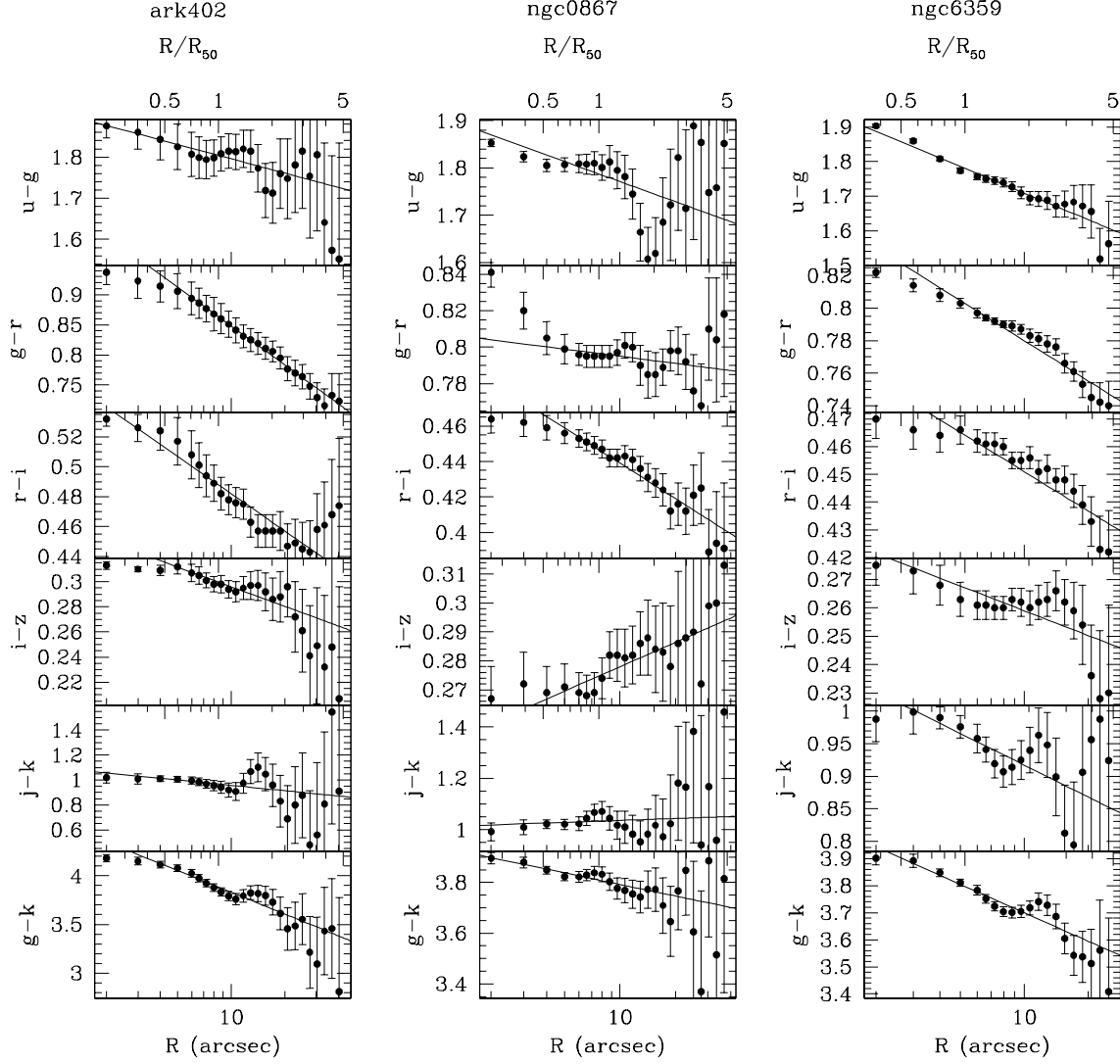


Fig. 6.— Examples of optical and NIR color profiles (color versus the radius of isophote annulus) for galaxies Ark 402, NGC 0867 and NGC 6359. The line in each panel is the best fit of the color profile. The radius in unit of  $R_{50}$  (the SDSS  $r$ -band) is also labelled for the corresponding galaxies.

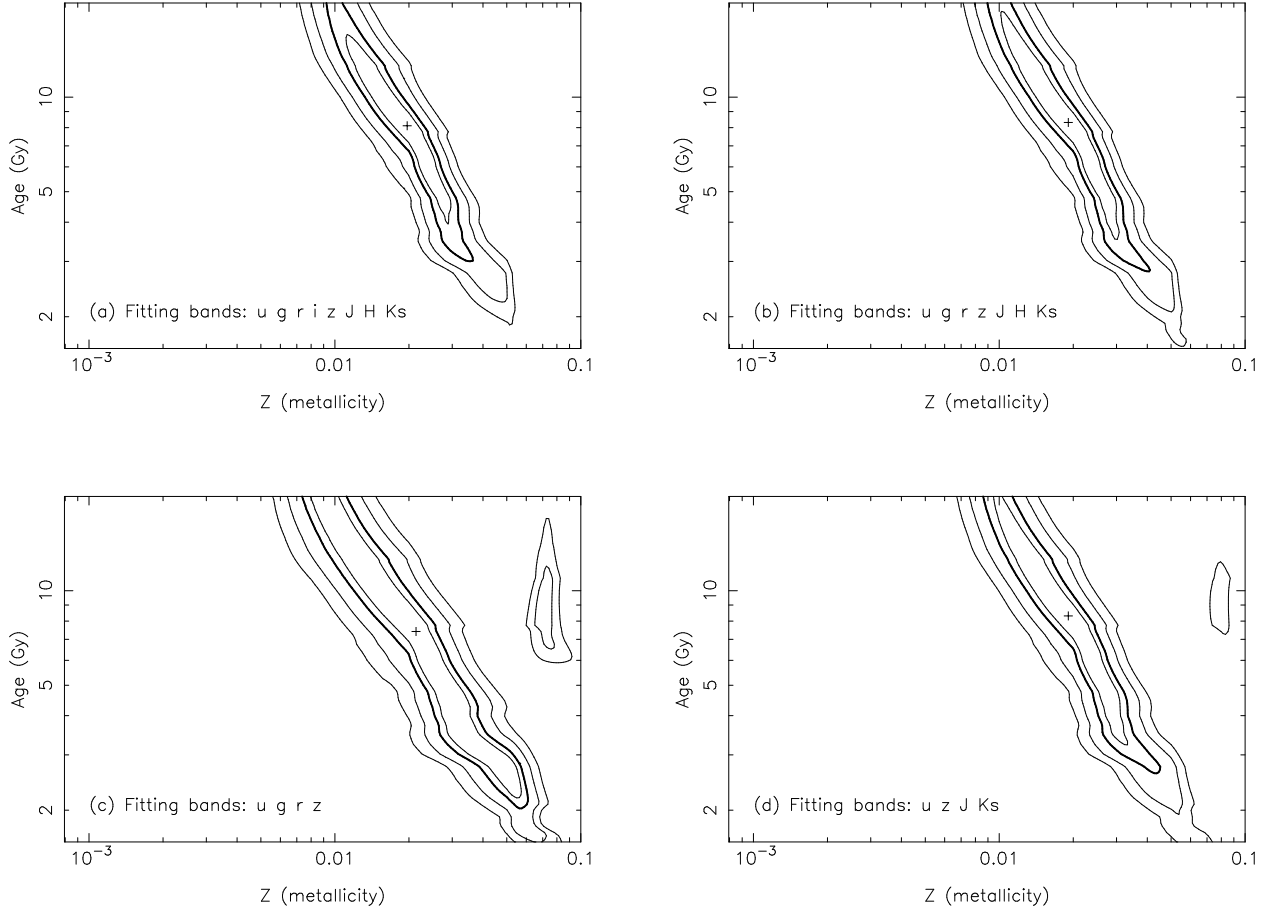


Fig. 7.— The contours of  $\Delta\chi^2$  for a simple stellar population with  $\text{Age} = 8.0\text{Gyr}$  and  $Z_{\text{met}} = 0.02Z_{\odot}$ . Uncertainties of magnitude in individual bands are chosen to be the typical values of our sample;  $\sigma_{\text{obs}} = 0.05, 0.01, 0.01, 0.01, 0.02, 0.07, 0.08, 0.11$  mag for  $u, g, r, i, z, J, H, K_S$ , respectively. A model error of  $\sigma_{\text{mod}} = 0.05$  mag is also included. The thick lines have  $\Delta\chi^2 = 2.30$ , correspond to 68.3% confidence level, and the 2 outer contours correspond to 95.4% and 99.7% respectively. The innermost lines have  $\Delta\chi^2 = 1.0$ , that indicates the errors if only one of the parameters is fitted. Panel (a) shows the results obtained by using all the eight bands data; panel (b) uses all bands except  $i$ ; panel (c) uses only four SDSS bands (also except  $i$ ); panel (d) uses four bands that cover both SDSS and 2MASS wavelengths.

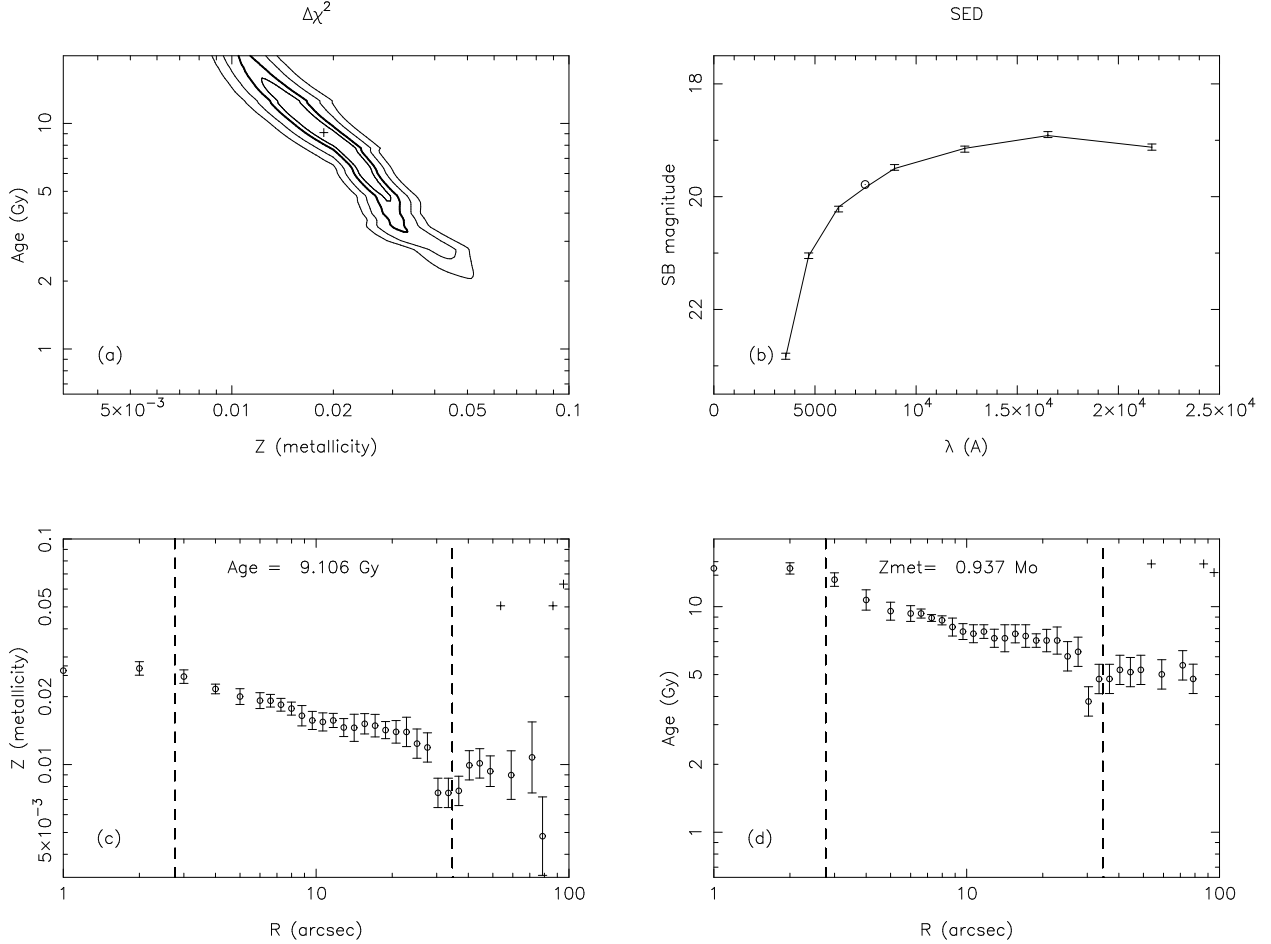


Fig. 8.— An example of the fit to the SED of NGC 4044. (a) shows the contour map of  $\Delta\chi^2$  for the fit of the SED at  $R_{50}$ . (b) shows the best fit SED, with the line showing the SED for a SSP with  $Z_{met} = 0.94Z_{\odot}$  and Age = 9.1Gyr. The omitted *i*-band is plotted as a circle in this figure. (c) presents the best fit  $Z_{met}$  values and their errors at different radii, where *Age* is forced to be the best fit value at  $R_{50}$ , i.e. 9.1 Gyr. (d) shows the best fit of *Age* at different radius, where  $Z_{met}$  is forced to be the best fit value at  $R_{50}$ , i.e.  $0.94 Z_{\odot}$ . Crosses in (c) and (d) indicate the failure of fitting at these radii because the quality of the observations is too low to give a meaningful constraint.

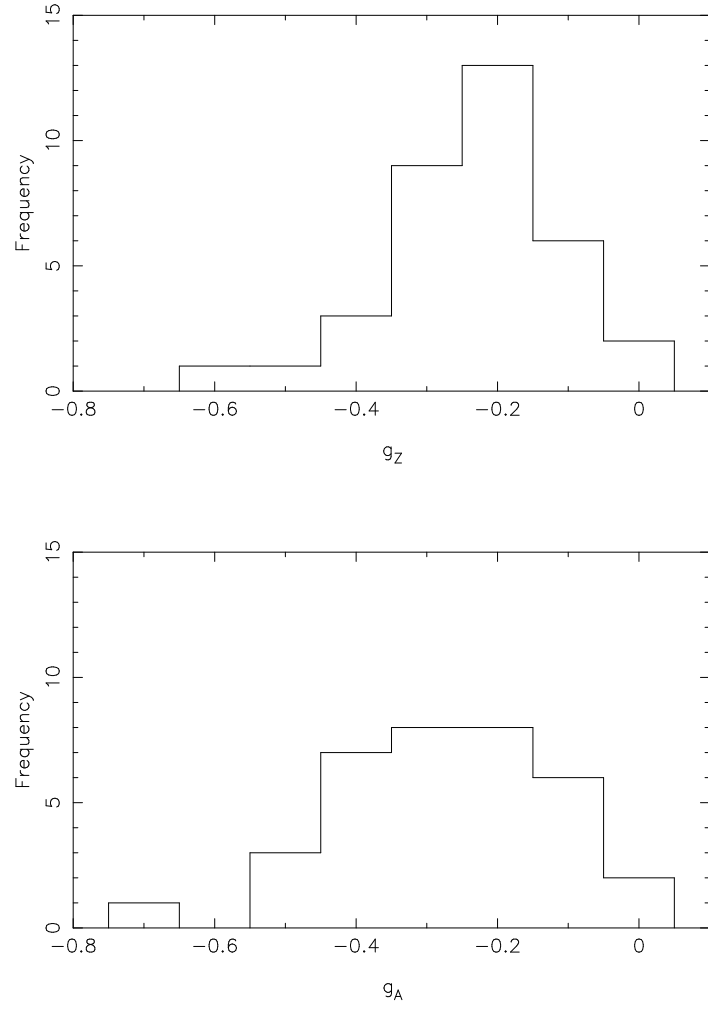


Fig. 9.— The distributions of the metallicity gradients  $g_Z$  (at upper panel) and the age gradients  $g_A$  (at lower panel), with the assumption of  $g_A \equiv 0$  and  $g_Z \equiv 0$  respectively. The median values are  $g_Z \approx -0.22$  and  $g_A \approx -0.31$  for all sample galaxies.

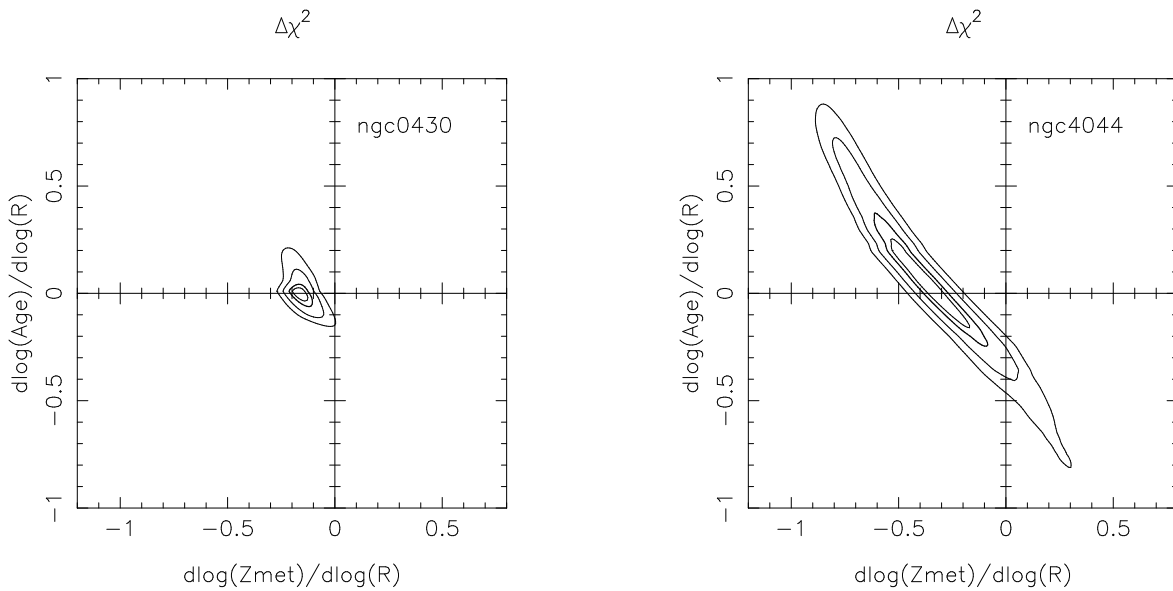


Fig. 10.— The contours of  $\Delta\chi^2$  in the  $g_Z - g_A$  space for for NGC 0430 and NGC 4044. The thick lines have  $\Delta\chi^2 = 2.30$ , correspond to 68.3% confidence level, and the 2 outer contours correspond to 95.4% and 99.7% respectively. The innermost lines have  $\Delta\chi^2 = 1.0$ , that indicate the errors if only one of the parameter is fitted.

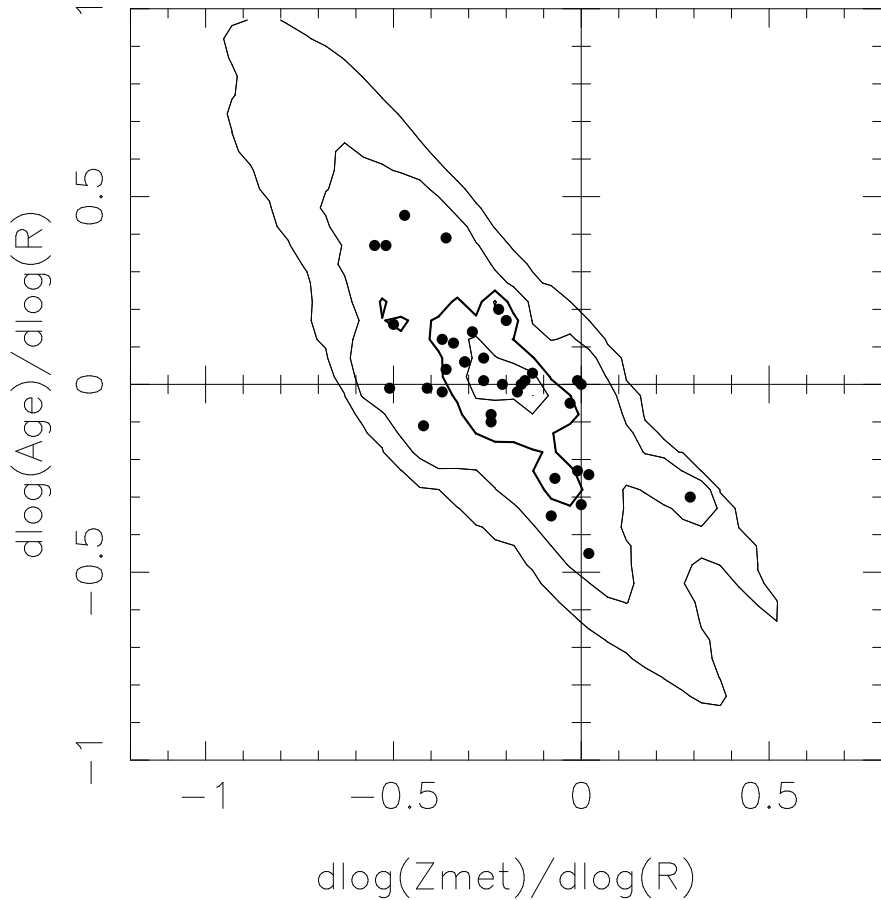


Fig. 11.— The distribution of  $g_Z$  and  $g_A$  obtained by fitting the observed SEDs with the SSP model. Solid points represent the best fit of individual galaxies. Contours show the relative number density of galaxies in this parameter space, and are obtained by summing up the possibility distribution of each galaxy derived from its  $\Delta\chi^2$  distribution [see figure 10 ]. The thick line is the contour which circles 68.3% possibilities of the total galaxy number, while the other two lines show the 95.4% and 99.7% regions.

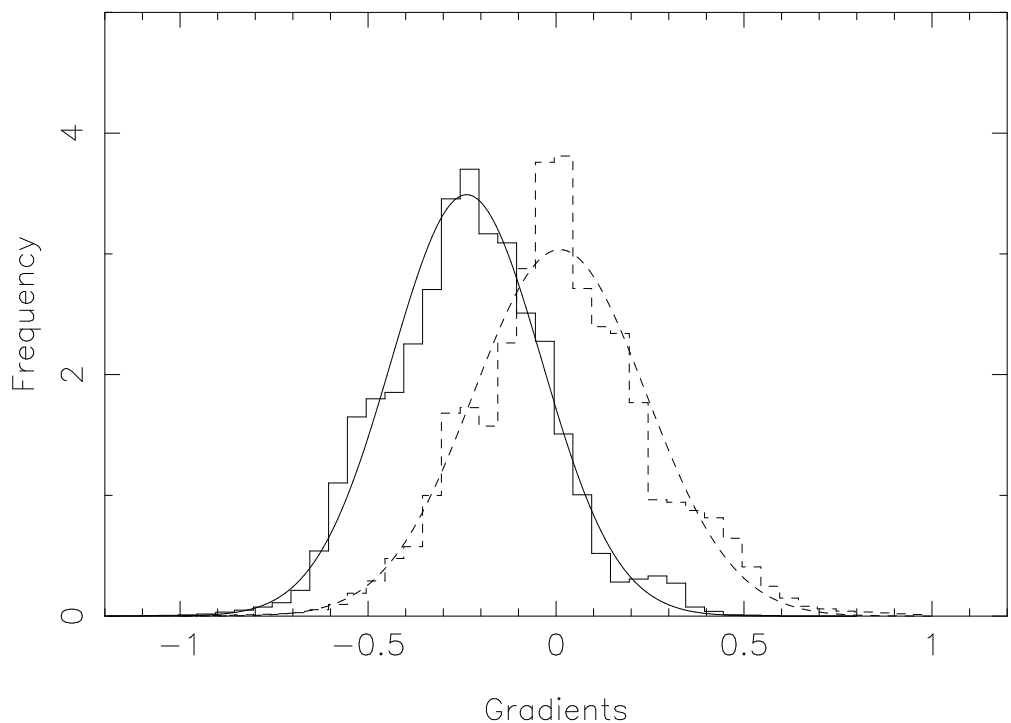


Fig. 12.— The projection of the distribution shown in Figure 11 onto the  $g_Z$  (solid histogram) and  $g_A$  (dashed histogram) axis. Smoothed curves show the best fits to gaussian distribution.

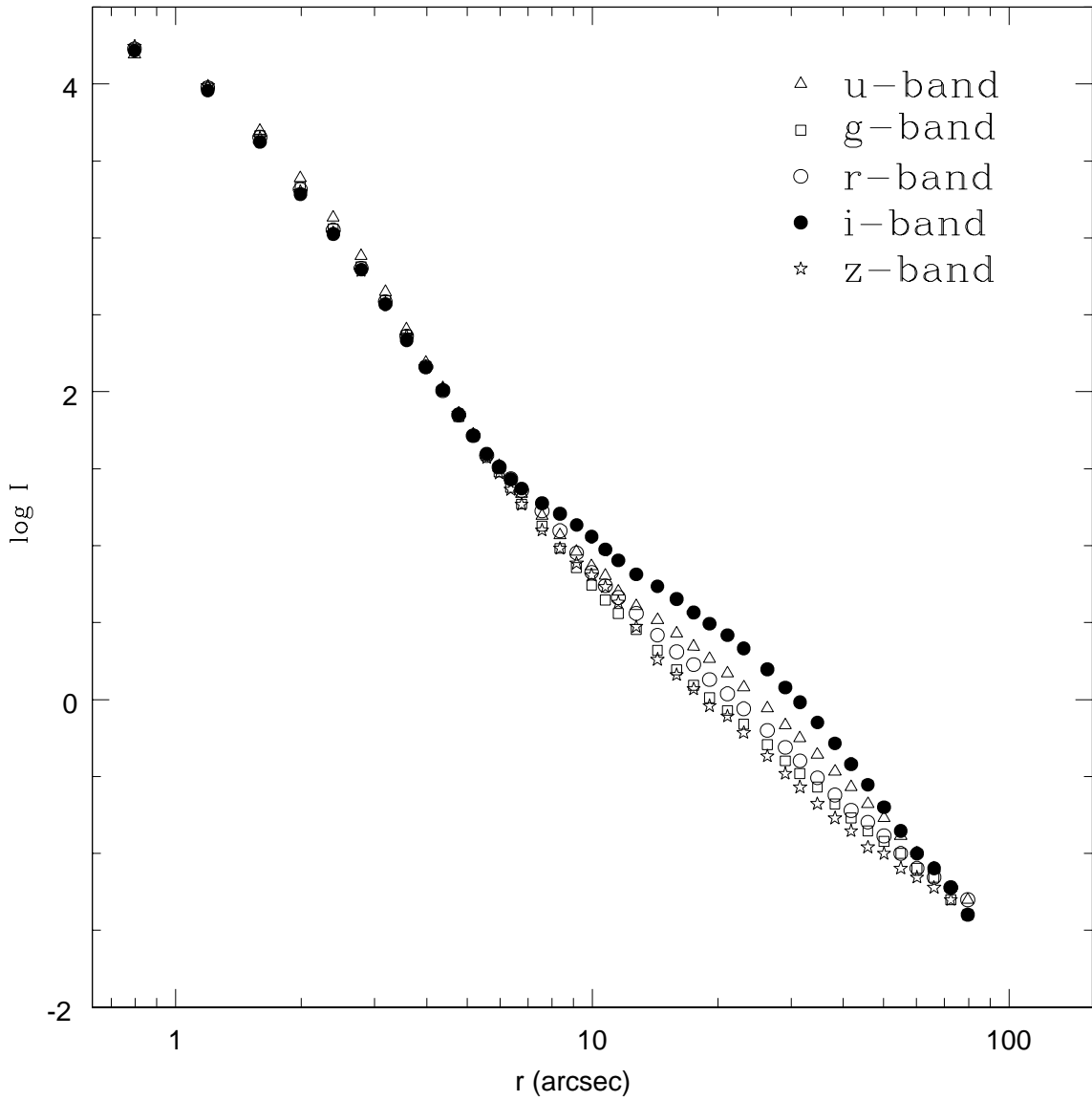


Fig. 13.— The radial profiles of the averaged PSFs in the five SDSS bands. All the PSF profiles are scaled and plotted with different symbols. The red halo of the PSF is clearly seen in the  $i$ -band. It produces a bright wing that is the most prominent in the radius range 10 - 50 arcsec.

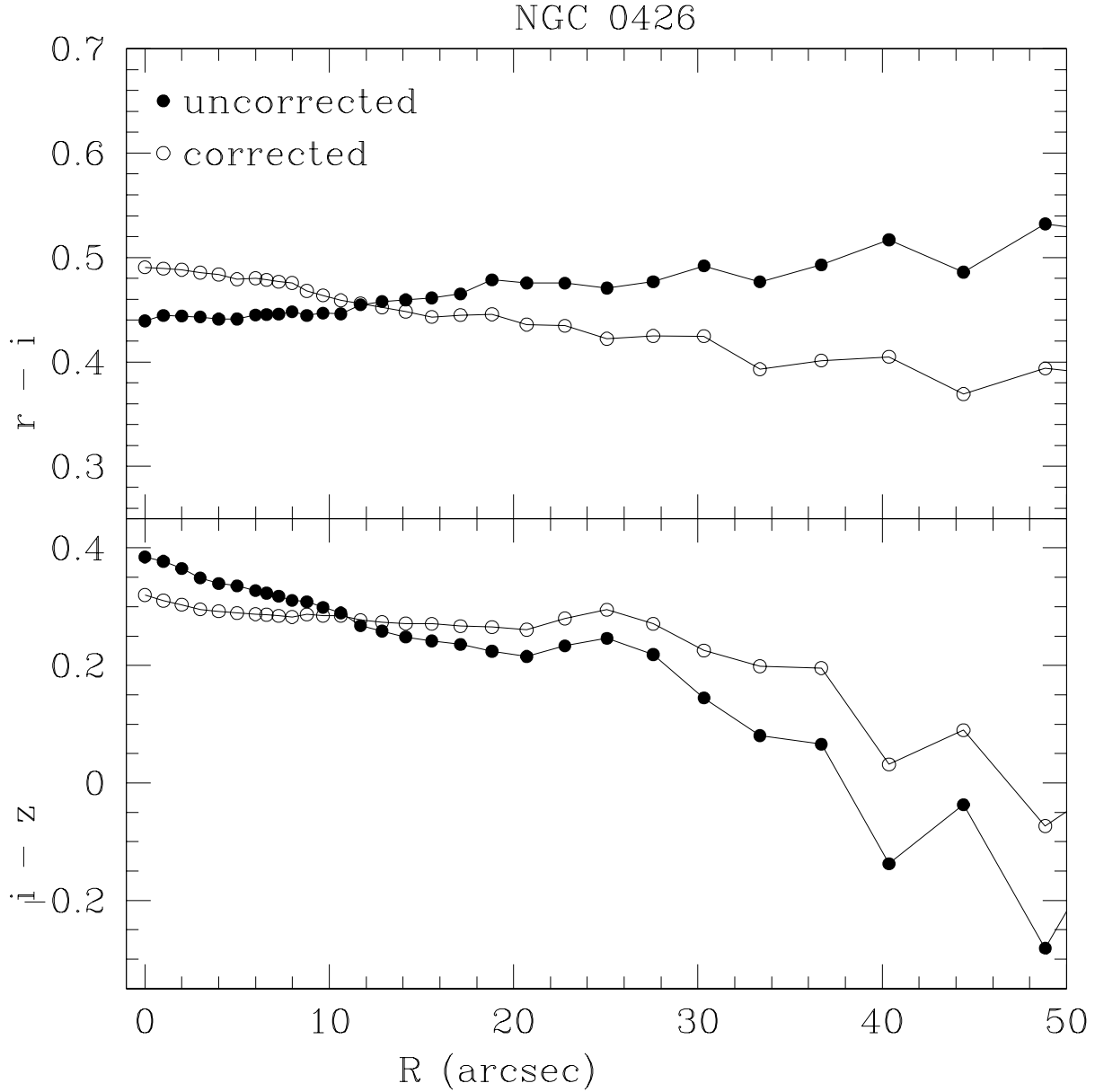


Fig. 14.— The profiles of  $r - i$  and  $i - z$  colors as a function of the isophote radius for galaxy NGC 0426. The filled and open points are the data before and after the correction of the ‘red halo’ effect. It is clear that the ‘red halo’ effect in the  $i$ -band biases significantly the  $r - i$  gradient.